

Relativistic MHD simulations of core-collapse GRB jets: 3D instabilities and magnetic dissipation

Omer Bromberg^{1*}†, Alexander Tchekhovskoy^{3,4‡}

¹Department of Astrophysical Sciences, Peyton Hall, Princeton University, Princeton, NJ 08544, USA

²Departments of Astronomy and Physics, Theoretical Astrophysics Center, University of California Berkeley, Berkeley, CA 94720-3411

³Lawrence Berkeley National Laboratory, 1 Cyclotron Rd, Berkeley, CA 94720, USA

Accepted. Received; in original form

ABSTRACT

Relativistic jets are a natural outcome of some of the most violent and spectacular astrophysical phenomena, such as the core collapse of massive stars in gamma-ray bursts (GRBs) and the accretion onto supermassive black holes in active galactic nuclei (AGN). It is generally accepted that these jets are powered electromagnetically, by the magnetised rotation of a central compact object (a black hole or neutron star). However, how the jets produce the observed emission and survive the propagation for many orders of magnitude in distance without being disrupted by current-driven non-axisymmetric instabilities is the subject of active debate. We carry out time-dependent 3D relativistic magnetohydrodynamic simulations of relativistic, Poynting flux dominated jets that propagate in a spherically-symmetric power-law density distribution. The jets are launched self-consistently by the rotation of a strongly magnetised central compact object. This determines the natural degree of azimuthal magnetic field winding, a crucial factor that controls jet stability. We find that the jets are susceptible to two types of instability: (i) a global, *external kink* mode that grows on long time scales and causes the jets to bodily bend sideways. Whereas this mode does not cause jet disruption over the simulated distances, it substantially reduces jet propagation speed. We show, via an analytic model, that the growth of the external kink mode depends on the slope of the ambient medium density profile. In flat density distributions characteristic of galactic cores, an AGN jet may stall, whereas in stellar envelopes the external kink weakens as the jet propagates outward; (ii) a local, *internal kink* mode that grows over short time scales and causes small-angle magnetic reconnection and conversion of about half of jet electromagnetic energy flux into heat. Based on the robustness and energetics of the internal kink mode, we suggest that this instability is the main dissipation mechanism responsible for powering GRB prompt emission.

Key words: stars: magnetic field – stars: neutron – pulsars: general – stars: rotation.

1 INTRODUCTION

Relativistic jets are ubiquitous among astrophysical systems that involve accretion onto compact objects, such as gamma-ray bursts (GRBs), active galactic nuclei (AGNs) and microquasars (see, e.g. a review by Levinson 2006). It is commonly agreed that these jets are powered electromagnetically, most likely by the winding of magnetic field lines that thread a rotating central compact object (Blandford & Znajek 1977; Komissarov 2001; Tchekhovskoy et al. 2010a). The winding generates a Poynting flux dominated outflow, which eventually becomes the jet, at the expense of the rotational energy of the central engine. Although significant progress has been made recently in understanding how jets are formed

magnetically (see, e.g., Tchekhovskoy 2015 for a review), their physics, most notably the stability properties and the energy dissipation mechanisms, is the subject of active debate. In the context of non-relativistic jets, the expectation is that magnetised jets are strongly unstable to current-driven instabilities. For instance, Moll et al. (2008); Moll (2009) show that non-relativistic jets readily develop current-driven, non-axisymmetric, kink ($m = 1$) modes whose properties depend on the conditions at the jet base. In the core collapse of a massive star, heavily mass-loaded jets, which are produced by the rotation of a protoneutron star (Burrows et al. 2007), were found to be so strongly unstable to the kink instability that they were unable to penetrate the star (Mösta et al. 2014).

If this instability were to extend also to the relativistic, highly magnetised jets this would have serious implications on the properties of relativistic jets and the engines that launch them. In the context of long-duration GRBs (Woosley 1993; MacFadyen & Woosley 1999) it would imply that magnetised jets are unable to

* E-mail: omerb@astro.princeton.edu

† Lyman Spitzer, Jr. Fellow

‡ Einstein Fellow

break out of the star, a necessary condition to form a GRB. Therefore, it would mean that GRB jets have to be created *unmagnetised*, making it impossible to power them by the electromagnetic spin-down of the central object. However, the observed properties of relativistic jets suggest otherwise. For example, the high power observed in GRB and AGN jets significantly challenges the known non-magnetic energy extraction mechanisms available in these objects (e.g. Phinney 1982; Kawanaka et al. 2013; Leng & Giannios 2014). Moreover, a recently discovered correlation between the jet magnetic field strength and the accretion disc luminosity in AGN (Zamaninasab et al. 2014), and several surprising features that are seen in GRB lightcurves and can be naturally produced by magnetic jets (Tchekhovskoy & Giannios 2014) strongly support the magnetic origin of the jet power.

On the other hand if the magnetic jets were mostly stable it would be difficult to explain the high energy emission radiated from them (see, e.g., McKinney & Blandford 2009; Narayan et al. 2009). In a stable jet about half of the energy remains locked in the magnetic form, out to very large distances (Tchekhovskoy et al. 2010b). In such a case internal shocks, which are commonly invoked to explain the observed high energy emission, are weak (Kennel & Coroniti 1984) and cannot accelerate efficiently the radiating electrons (e.g., Mimica et al. 2010; Narayan et al. 2011). Various alternative dissipation mechanisms have been discussed in this context, including striped wind like magnetic field configurations, which are susceptible to reconnection (e.g., Drenkhahn & Spruit 2002; Giannios & Spruit 2005; Metzger et al. 2011; McKinney & Uzdensky 2012), microphysical energy dissipation mechanisms (e.g., Beloborodov 2010; Mészáros & Rees 2011), and effects from intermittent engine (e.g. Granot et al. 2011). To date, no universally-accepted mechanism that is capable of efficiently converting jet magnetic energy into radiation exists. The presence of a local current-driven instability in a mildly unstable jet could be sufficient for triggering magnetic dissipation and powering the observed GRB emission (Lytikov & Blandford 2003; Giannios 2008, 2012). This motivates a focused, high-resolution study of jet stability in the context of core-collapse GRB jets.

Current-driven instability is mainly a 3D effect and can be highly non-linear. Thus 3D simulations are needed to study it. The standard approach for simulating magnetic jets is sending loops of magnetic field into the computational domain at a fixed rate (e.g., Mignone et al. 2010; Guan et al. 2014). In this case, the strengths of the poloidal magnetic field component, B_p (i.e., lying in the plane passing through the jet axis), and azimuthal component, B_ϕ (perpendicular to the plane), are arbitrary. However, jet stability depends sensitively on the ratio between the two (Appl et al. 2000; Narayan et al. 2009; Mizuno et al. 2012). Thus, the results of such jet “injection” simulations reflect a particular (arbitrary) choice for the injection boundary condition, making it difficult to interpret them. Lately, Bromberg et al. (2014) showed analytically that Poynting-dominated jets that form at the center of collapsing stars are at least marginally stable and can punch through the stellar envelope without being disrupted by magnetic instability. However, in the absence of a full 3D numerical simulation, they had to assume a ratio between B_ϕ and B_p , and did not address the question of magnetic energy dissipation.¹

¹ They employed a linear analysis and assumed that the strengths of the toroidal and poloidal field components are comparable (in the fluid frame). Such an assumption is usually attributed to jets that propagate through a pre-evacuated funnel and is commonly used in the studies of jet stability (e.g., Narayan et al. 2009; McKinney & Blandford 2009).

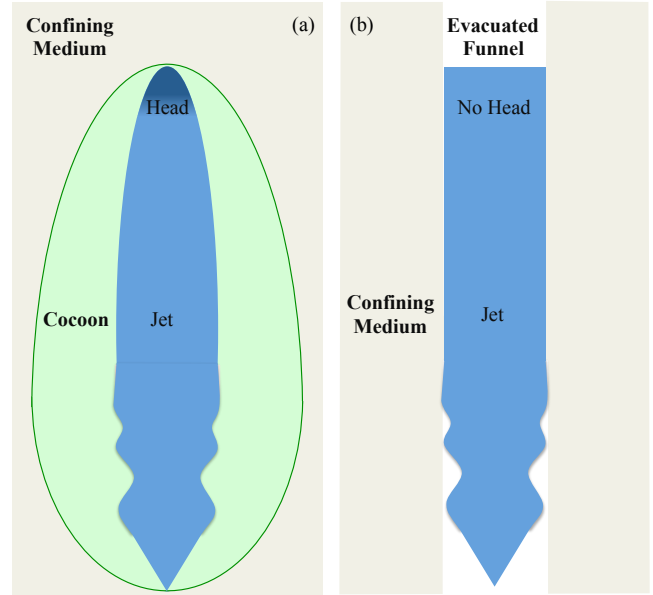


Figure 1. A schematic view of a headed jet (panel a) that propagates in an ambient medium, and a headless jet (panel b) that propagates in a preexisting evacuated funnel. As the headed jet runs into the ambient gas, it slows down, its toroidal magnetic flux accumulates and grows in strength, and its outermost parts form a head (shown in dark blue), a working surface at which the jet drills through the ambient gas and in which the magnetic field strength is enhanced. This causes the formation of a bow shock (shown with the dark green line), and the shocked ambient gas forms the cocoon (shown in green) that collimates the jet into a cigar-like shape. In contrast, a headless jet has no ambient gas to push through and is free to propagate along a pre-evacuated funnel. It propagates faster than headed jets and assumes the shape dictated by the funnel and/or ambient pressure profile. Because headless jets do not have to push through the ambient gas, their toroidal field is weaker and they are more stable to kink instabilities than headed jets.

In nature, the strengths of the poloidal and toroidal magnetic field components are tightly connected. This is because the jets are produced by the rotation of magnetised compact objects, so B_ϕ emerges from the winding of B_p . The winding creates an outward Poynting flux. In the presence of an ambient medium, which confines the electromagnetic outflow, the magnetic tension of the azimuthal field builds up, until it focuses the outflow into twin polar collimated jets (Lynden-Bell 1996), as illustrated in Fig. 1(a). These jets start propagating once their pressure becomes high enough to push the ambient medium aside. As the jet propagates, it develops a slow-moving “head”: a working surface at which the jet drills through the ambient material and which is shown in Fig. 1(a) in dark blue. The head blocks the free expansion of the toroidal magnetic flux in the jet and keeps the jet toroidal magnetic pressure high. As a result, the jet pushes against the head with a greater force. We term this type of jets *headed jets*. The relative strength of toroidal and poloidal fields in the jet is therefore linked with the properties of the ambient medium that collimates it. Thus, any attempt to analyse jet stability should take into consideration the presence of the ambient medium and its effect on the jet magnetic field configuration.

Jets that expand into a pre-existing, evacuated funnel are of different nature. They are free to accelerate to super fast-magnetosonic velocities, as illustrated in Fig. 1(b). The tip of the latter jets cannot communicate backward, and the jet material behaves as if it were part of an infinite jet. In these jets, the

toroidal and poloidal fields can be in equipartition in the fluid frame (Tchekhovskoy et al. 2008; Lyubarsky 2009, 2011). We term these jets *headless* jets to distinguish them from the headed jets discussed above.

In this work we address two important questions in the physics of magnetised GRB jets: the stability of the jet as it propagates in the star and the dissipation of its magnetic energy. We present the results from a numerical study of the formation and propagation of relativistic Poynting flux dominated jets in a dense medium typical for a GRB progenitor star. The jets are formed by the rotation of a magnetised neutron star (NS) with a super-strong magnetic field, or a magnetar, in the same manner as described earlier. Thus, the magnetic field configuration is generated self-consistently, without any ad hoc assumptions about the ratio between B_ϕ and B_p . This allows us to study jet stability from first principles. Note that even though we focus on GRB jets, our results are general and apply to relativistic jets in other astrophysical systems, such as AGN jets.

We start by describing our numerical scheme and the problem setup (Section 2) and reviewing the main aspects of kink instability in magnetically-dominated jets (Section 3). We then discuss the difference between headless jets, which are launched into a pre-existing funnel (Section 4), and headed jets, which drill their way through a dense ambient medium (Section 5). We show that while headless jets are relatively stable to kink modes, headed jets are kink-unstable. In Section 6, we analyse the results of our 3D jet simulations and discuss the effect that the kink instability has on the jets and the limitations of our work. We then construct an analytic model that describes the jet properties (Section 7). In Section 8, we discuss the astrophysical implications for GRB and AGN jets. We finish by comparing our results to previous works done on the subject (Section 9) and conclude (Section 10). Throughout this paper, we use both spherical (r, θ, ϕ) and cylindrical (R, ϕ, z) coordinates.

2 NUMERICAL SCHEME, UNITS, AND PROBLEM SETUP

We carry out our simulations using the **HARM** code (Gammie et al. 2003), with recent improvements (McKinney 2006; Tchekhovskoy et al. 2007, 2009; McKinney & Blandford 2009; Tchekhovskoy et al. 2011). This is a static mesh, 3D, general relativistic magnetohydrodynamic (GRMHD) code capable of following the evolution of high magnetisation flows while conserving mass, energy and momentum to machine precision. An important advantage of the code is its ability to use curved grids, as we explain below.

We run both 2D (axisymmetric) and 3D simulations on a grid that spans a range $(r_{\text{in}}, r_{\text{out}}) \times (0, \pi) \times (0, 2\pi)$ in spherical polar coordinates, (r, θ, ϕ) . We set the boundary conditions to be reflecting at the poles ($\theta = 0, \pi$), free streaming at the outer radial boundary ($r = r_{\text{out}}$), and periodic in the ϕ -direction. The radial grid is uniformly spaced in $\log r$ out to the radius r_{br} , beyond which the grid becomes progressively sparse. Tables 1 and 2 summarise the parameters of different models we use in this work, and we give more details in the corresponding sections.

At the inner radial boundary ($r = r_{\text{in}}$), we place a perfectly conducting sphere carrying a monopole magnetic field. At the beginning of the simulation, the sphere is instantaneously spun up to a constant angular frequency. This generates Poynting flux dominated outflow that emanates from the surface of the sphere. We spin the inner sphere at a rather large angular frequency $\Omega \sim 0.5c/r_{\text{in}}$ so that the light cylinder, the cylindrical radius at which co-rotation

velocity equals the speed of light,

$$R_L \equiv \frac{c}{\Omega}, \quad (1)$$

is a few times r_{in} . This allows us to speed up the simulation while keeping the physics the same (Komissarov et al. 2007). Outside the sphere we set a static background density that resembles the interior of a star. The ambient density is a continuous single power-law distribution $\rho_a = r^{-\alpha}$ that extends between an inner “bubble” of radius $r_b \geq r_{\text{in}}$ and the outer radius of the grid. We will focus in this work on $\alpha = 2.5$, a value of power-law index that is characteristic of Wolf-Rayet stars (e.g. Heger et al. 2000). We assume cold medium, ignore gravity,² and do not impart any perturbations to the initial conditions.

Numerical MHD codes cannot evolve vacuum of density. Therefore, we set the boundary condition at $r = r_{\text{in}}$ and the initial density ρ in the region between r_{in} and r_b by demanding that the terminal Lorentz factor of the flow, which is controlled by the initial magnetisation of the flow, is $\Gamma_\infty = \sigma_0 = b^2/4\pi\rho c^2 = 25\text{--}50$. This value is high enough ($\gg 1$) to lead to a relativistically-magnetised outflow and at the same time low enough to keep the numerical noise to a minimum.

In the context of GRBs, we normalise all length scales by $R_L = 10^7$ cm, the light cylinder radius of a 2 ms NS; the magnetic field strength by $B_L = 10^{13}$ G, the magnetic field on the light cylinder; and all energy and density terms by $B_L^2/4\pi$. Time is measured in the units of light crossing time of the light cylinder, $R_L/c = 0.33$ ms. In these units, the dimensionless 3-velocity $\beta \equiv v/c = z/t$. The fiducial value of density, $\rho_{L,\text{fid}}^a = 4500$, corresponds to jets of power 7×10^{49} erg s^{-1} propagating in a $10M_\odot$ star. In the context of AGNs, one can use a light cylinder of 1.5×10^{13} cm and a magnetic field of $B_L \simeq 10^5$ G that correspond to a maximally rotating supermassive black hole (BH) of mass $10^8 M_\odot$. The fiducial density in these units corresponds to $\sim 10^{-7}$ g cm^{-3} at the light cylinder (see Table 2). Unless mentioned otherwise, we will give physical units in the text in the context of GRB jets.

Table 1 summarises the parameters of the numerical grid we used to carry out the simulations, while Table 2 lists the physical parameters of the setup, giving them in dimensionless units as well as physical units specialised to GRBs and AGNs. The essential parameters that control the jet stability are given in the first two columns of Table 2: (i) the dimensionless magnetic field energy density (in units of ambient density), $\propto B_L^2/\rho_L c^2$, which is a proxy for jet power L_j , and (ii) the power-law index of the ambient density distribution, α . The third parameter, $\propto L_j/B_L^2 R_L^2$, reflects the fraction of the stellar surface area that launches the outflow, which is slightly different in 2D and 3D simulations, as we discuss below. The fourth parameter, σ_0 , sets the initial magnetisation of the outflow and does not influence the simulation outcome so long as $\sigma_0 \gg 1$: it affects the results only at larger distances than those simulated here (e.g., outside the star).

2.1 2D simulation setup

We carry out our 2D simulations on a spherical polar grid that is modified to concentrate grid cells toward the polar axis, where the

² Whereas gravity and ambient pressure may be important close to the jet launching point, they become less important at larger distances that are the main focus of this work. For instance, the free-fall time scale of the outer parts of the star is of order of 100 s, which is much longer than the time it takes for the jet to pierce the star, as we will show.

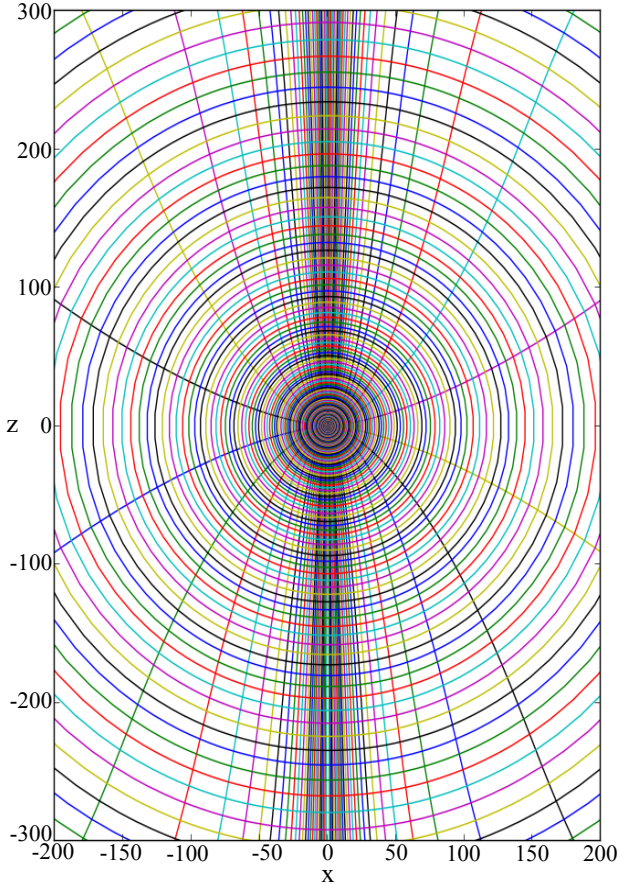


Figure 2. The shape of the grid lines used in our 2D (axisymmetric) simulations (for clarity, we show every fourth grid line). The grid lines collimate toward the rotational axis (the z -axis) thereby concentrating the resolution in the body of the jet. In the 3D simulations, the collimation is performed toward the x -axis to avoid the interaction of the jets with the coordinate singularity (see Sec. 2.2), with the θ and ϕ angles of the grid lines deformed independently, in the same way θ -lines are deformed in the Figure.

jets form, by deforming the radial grid lines into parabolae, as seen in Fig. 2. We direct the rotational axis along the polar axis ($\theta = 0$) and use a resolution of $1024 \times 256 \times 1$ in the r -, θ - and ϕ - directions, respectively (see Table 1). At this resolution the light cylinder ($R_L = 2r_{in}$) is resolved by 5 cells, at an altitude $|z| = 1000r_{in}$, and the jet width by 40 cells. We ran the simulations with both dipole and monopole magnetic field geometries and verified that in both cases the resultant jet properties are qualitatively the same. This is because in both cases the jet field lines stretch from the central source to the jet head and return back to the source (see Section 5). The only essential difference is that in the dipole case there is a region of closed field lines around the equator of the central object, which modify the conditions near the base of the jet (Tchekhovskoy et al. 2015). We verified that for an aligned rotator, this effect does not substantially affect the properties of the jet at higher altitudes. We will therefore restrict ourselves to the monopole field. This choice corresponds to the assumption of a large-scale magnetic flux threading the progenitor star (Bucciantini et al. 2009).

Table 1. Simulation grid parameters for the various models we present in this paper. See Sec. 2 for the description of the parameters in the table.

Model name	Resolution ($N_r \times N_\theta \times N_\phi$)	$\frac{r_{in}}{R_L}$	$\frac{r_b}{R_L}$	$\frac{r_{br}^*}{R_L}$	$\frac{r_{out}}{R_L}$
M2	$1024 \times 256 \times 1$	0.5	2	500	5000
M2Cyl	$1024 \times 256 \times 1$	0.5	2	500	5000
M3	$128 \times 96 \times 192$	0.8	0.8	800	8000
M3HR	$256 \times 192 \times 384$	0.8	0.8	800	160
M3LP	$128 \times 96 \times 192$	0.8	0.8	800	8000

* The radius beyond which the radial grid becomes progressively sparse.

2.2 3D simulation setup

In the 3D runs we use a slightly modified configuration of grid lines and magnetic field topology. The existence of a polar coordinate singularity in the grid along the z -axis leads to numerical difficulties when matter and magnetic fields pass through the pole. As a result, magnetic field lines cannot cross the pole freely and get wrapped around the z -axis. This is not a problem in the 2D case, since all quantities have azimuthal symmetry, and no mass, momentum, or energy flows through the pole. However in the 3D case, we found that the imperfect flow through the axis leads to an artificial stability of the jets. To avoid this non-physical behaviour, we opted for reorienting the rotational axis of the central object to point along the x -direction (see, e.g., Moll et al. 2008), and we collimate the radial grid lines along the x -axis accordingly. Namely, the collimation is performed such that the θ - and ϕ -angles of the radial grid lines deformed independently. Note that when reporting the simulation results, we will use the natural coordinate system set by the jet orientation, with the z -axis pointing along the rotational axis.

To avoid sending any fluxes through the z -axis, we spin not the entire star but only its northern and southern polar regions that are within 70° of the rotational axis. The rotation is uniform within 50° of the axis and smoothly tapers off down to zero at 70° . We run 3D simulations at two resolutions: a fiducial resolution of $128 \times 96 \times 192$ cells in the r -, θ -, and ϕ -directions, respectively, and a high resolution, for which the resolution is doubled in all 3 dimensions (see Table 1).

3 JET STABILITY AND ACCELERATION

Magnetically-dominated flows are subject to various types of instabilities. In a narrow jet, the fastest growing instability is the kink ($m = 1$) instability (Begelman 1998; Lyubarskii 1999). It excites large scale helical motions in the jet and can lead to the dissipation of the magnetic energy or even the disruption of the entire jet. Here and below, we will use \mathbf{b} for the magnetic field in the proper fluid frame and \mathbf{B} for the magnetic field in the lab frame.

The instability evolves on a time scale that is of the order of the Alfvén travel time around the unstable region. Suppose a jet consists of an inner core, which is located at $R \leq R_0$ and dominated by the poloidal field, $\mathbf{b}_p \equiv b_R \hat{\mathbf{e}}_R + b_z \hat{\mathbf{e}}_z$, and an outer region, which is dominated by the toroidal field, b_ϕ . Here, b_p and b_ϕ are the poloidal and toroidal field components measured in the proper frame, respectively. By construction, the pitch angle of the magnetic field in the proper frame, b_p/b_ϕ , is of order unity at the edge of the core. Then, the growth timescale of the fastest growing kink mode in the

Table 2. The physical parameters of the various models we present in this paper. The two essential parameters describing the astrophysical system are the first two ones: the dimensionless magnetic field energy density (in units of ambient density) and the ambient density slope. See Sec. 2 for the description of the parameters in the table. Unless otherwise noted, cgs units are used.

Model name	Scale-free parameters				GRB-scaled par.				AGN-scaled parameters				
	$\frac{4\pi\rho_L c^2}{B_L^2}$	α	$\frac{3L_j}{B_L^2 R_L^2 c}$ †	σ_0 ‡	$\frac{P}{\text{ms}}$	$\frac{R_L}{10^7}$	$\frac{L_j^\diamond}{10^{49}}$	$\frac{M}{M_\odot}$	a_{BH}	$\frac{M_{\text{BH}}}{10^8 M_\odot}$	$\frac{R_L}{10^{13}}$	$\frac{L_j^\diamond}{10^{46}}$	$\frac{\rho_L}{10^{-7}}$
M2	4500	2.5	1	50	2	1	7	10	1	2.5	1.5	2.3	3
M2Cyl	10^5	0	1	50	2	1	7	10	1	2.5	1.5	2.3	3
M3	4500	2.5	0.76	25	2	1	5	10	1	2.5	1.5	1.7	3
M3HR	4500	2.5	0.76	25	2	1	5	10	1	2.5	1.5	1.7	3
M3LP	45000	2.5	0.76	25	2	1	0.5	10	1	2.5	1.5	0.17	3

† The total Poynting flux from a rotating monopole field is $2B_L^2 R_L^2 c/3$

‡ Defined as $b^2/4\pi w$ at the base of the jet, where $w \equiv \rho + u + p$ is the enthalpy density.

◇ L_j denotes the power of a single jet.

lab frame is (e.g. Appl et al. 2000):

$$t_{\text{kink}} \simeq \frac{2\pi R_0 \gamma_j}{v_A} \frac{b_p}{b_\phi}, \quad (2)$$

where γ_j is the bulk Lorentz factor of the flow and v_A is the Alfvén velocity,

$$\frac{v_A}{c} = \frac{b}{\sqrt{b^2 + 4\pi w}}, \quad (3)$$

with $b = (b_\phi^2 + b_p^2)^{1/2}$ being the total field strength in the fluid frame, $w \equiv \rho + u + p$ the plasma enthalpy, and u and p gas internal energy and pressure, respectively.

From eq. (2) we see that strong toroidal fields tend to destabilise the jet and lead to the growth of kink instability, whereas strong poloidal fields tend to stabilise the jet against kinking. Typically, it takes about 5–10 growth times for the instability to evolve to sufficiently affect the global structure of the magnetic field. Mizuno et al. (2012) found that the instability growth time is linked with the transverse profile of the fluid frame toroidal magnetic field. Kink modes grow faster in steep profiles e.g. $b_\phi \propto R^{-1}$, while in shallower profiles the instability takes longer to grow. Relativistic motions increase the growth time in the lab frame even further due to the time dilation, as evident in eq. (2), and therefore increase the stability against kink modes even further.

The fact that the growth of the kink modes requires Alfvén waves to travel several times around the jet, implies that fluid elements must be able to communicate efficiently across the jet; otherwise the instability cannot grow. In a highly magnetised flow, with $b^2 \gg 4\pi w$, we have $v_A \simeq c$ (eq. 3), for which the condition for strong causal contact is (Lyubarskij 1992):

$$\gamma_j \theta_j \lesssim 1. \quad (4)$$

Equation (4) states that a fluid element with a Lorentz factor γ_j moving along a field line that makes an angle θ_j with the jet axis, can communicate with the jet axis in a time that is shorter than the time it takes it to double its altitude. Only those regions in the jet that are strongly causally connected with the axis can become kink unstable (Lyubarskij 1992; Porth & Komissarov 2015).

4 AXIALLY SYMMETRIC HEADLESS JETS: JETS MOVING THROUGH LOW-DENSITY MEDIUM

It is convenient to study highly magnetised jets in the force-free approximation (e.g. Beskin et al. 2004; Narayan et al. 2007;

Lyubarsky 2009; Tchekhovskoy et al. 2008; Bromberg et al. 2014). In this approximation, gas inertia is neglected, and the motion of the plasma is given by the drift velocity of the electromagnetic field (Thorne et al. 1986; Beskin 1997; Narayan et al. 2007),

$$\beta_d = \left| \frac{\mathbf{E} \times \mathbf{B}}{B^2} \right| = \frac{E}{B}, \quad (5)$$

where \mathbf{E} is the electric field vector in the lab frame. In this section we consider *headless* jets that are free to move along a pre-existing evacuated funnel. In such jets, the lab-frame toroidal magnetic field can be approximated as (Beskin 1997; Narayan et al. 2007; Tchekhovskoy et al. 2008),

$$-B_\phi \simeq E = \Omega R B_p / c, \quad (6)$$

where Ω is the angular frequency of the central object, and $B_p \equiv (B_r^2 + B_z^2)^{1/2}$ and B_ϕ are the lab-frame magnetic field strengths of the poloidal and toroidal components, respectively. Plugging eq. (6) into eq. (5), we obtain the Lorentz factor,

$$\frac{1}{\gamma_j^2} = (1 - \beta_d^2) = \frac{B_p^2 + B_\phi^2 - E^2}{B^2} \simeq \frac{b_p^2}{B^2} + \frac{b_\phi^2}{B^2}, \quad (7)$$

where we approximate $B_p \simeq b_p$ and $b_\phi^2 \simeq B_\phi^2 - E^2$, since the motions are mostly in the poloidal direction. In the limit $b_\phi \lesssim b_p$ we can approximate:

$$\gamma_j \simeq \sqrt{1 + \frac{B_\phi^2}{B_p^2}} \simeq \sqrt{1 + \frac{R^2}{R_L^2}} \approx \frac{R}{R_L}. \quad (8)$$

The last approximate equality holds in the limit $R \gg R_L$, in which γ_j scales linearly with the cylindrical radius, similar to the acceleration in a hydrodynamic jet (Piran et al. 1993). The approximation $b_\phi \lesssim b_p$ which leads to eq. (8) holds close to the jet axis, where the plasma maintains strong causal connection ($\gamma_j \theta_j \lesssim 1$). If a jet is continuously collimated, the external collimating forces need to be communicated across the jet. This requires the jet to maintain a strong causal contact with the axis. Therefore, the linear growth of γ_j can only be maintained as long as $\gamma_j \theta_j \approx (R/R_L) \times \theta_j \lesssim 1$. At larger values of θ_j , the requirement that the external collimating force should be communicated across the jet cross-section limits the Lorentz factor to a value given by eq. (4), i.e. $\gamma_j \simeq 1/\theta_j$ (Tchekhovskoy et al. 2008, 2009; Lyubarsky 2009).

We now turn to the evaluation of jet stability to kink modes. In a steady state, there is a force balance in the transverse direction, at the jet inlet, between the magnetic pressure force and the

toroidal and poloidal hoop stresses, expressed via the following force-balance equation:

$$\frac{db^2}{8\pi dR} + \frac{b_\phi^2}{4\pi R} + \frac{E^2 - B_p^2}{4\pi R_{\text{curv}}} = 0, \quad (9)$$

where the first term is the magnetic pressure gradient, the second is the hoop stress of the toroidal field and the third is the hoop stress of the poloidal field, with R_{curv} denoting the poloidal curvature radius of magnetic field lines (see also Tchekhovskoy et al. 2008). A jet cannot be self-collimated and needs to be pressure supported on the outside by some external confining force (Eichler 1993; Tomimatsu 1994; Begelman & Li 1994; Beskin et al. 1998). In a jet that expands into a preexisting evacuated funnel, the force is dictated by the shape of the funnel walls. On the other hand, if the jet is pushing its way through an ambient medium, the confining force comes from a pressurised cocoon that is formed as a result of the jet propagation (see Fig. 1 and Sec. 5). The longitudinal (along the jet) pressure profile in the cocoon is relatively uniform and collimates the jet into a cylinder. This implies that the poloidal field lines are mostly along the z -direction, their curvature radius is very large, $R_{\text{curv}} \gg R$, and the third term in eq. (9) is negligible in comparison with the rest of the terms.

In order to solve eq. (9), we need to know the relationship between b_p and b_ϕ . Far from the jet axis, the velocity is mostly poloidal, and we can approximate $b_p \simeq B_p$ and

$$b_\phi \simeq \frac{B_\phi}{\gamma_j} \simeq \begin{cases} \left(\frac{R}{R_L}\right) b_p & , R \ll R_L, \\ b_p & , R \gg R_L, \end{cases} \quad (10)$$

where we used the eqs. (6) and (8) to connect B_ϕ and B_p . Thus, inside the light cylinder the magnetic field is dominated by the poloidal field, while outside the light cylinder the two are in equipartition, $b_p \simeq b_\phi$. Substituting this into eq. (9), we get that the profile of the toroidal field follows

$$b_\phi \propto \begin{cases} R & , R \ll R_L, \\ R^{-1/2} & , R \gg R_L. \end{cases} \quad (11)$$

Such a flat configuration of toroidal field outside R_L , was shown by Mizuno et al. (2012) to suppress the growth rate of kink modes. Moreover, the larger Lorentz factors decrease the lab-frame growth rate even further and result in a largely stable jet (see eq. 2). Making use of eq. (10), we obtain for the poloidal field,

$$b_p \propto \begin{cases} R^0 & , R \ll R_L, \\ R^{-1/2} & , R \gg R_L. \end{cases} \quad (12)$$

To illustrate the properties of headless jets, we run a 2D simulation with a rotating sphere threaded with a monopole magnetic field. The sphere is placed in an empty cylindrical funnel with a radius $R = 20$, carved out in a very dense ambient medium (see Table 2), where the medium plays the role of a rigid, confining wall. The funnel radius is set to be $R \gg R_L$ to allow for relativistic motions of the jet material. As we discussed in Section 1, the rotation of the central sphere generates toroidal field that expands outward as an Alfvén wave. The expansion is blocked by the confining medium, resulting in a buildup of toroidal tension which collimates the poloidal field lines toward the rotational axis (see Fig. 1b). The field lines undergo an initial oscillatory phase and relax into a cylindrical shape along the evacuated funnel (see Bogovalov & Tsinganos 2005 for a similar effect in a jet-sheath configuration). Outside the light cylinder, the jet material propagates outward super-Alfvénically and cannot communicate backward with Alfvén waves. Because of this, above the initial oscillatory phase, it behaves as part of an infinite, time-independent cylindrical jet.

A snapshot of the cylindrical jet is shown in Figure 3, where we show from left to right, meridional slices of b_ϕ , b_p , b_ϕ/b_p and $\gamma\beta$, respectively (the colour schemes show \log_{10} of the plotted parameters). Black solid lines track equal poloidal magnetic flux surfaces and follow the poloidal field lines. The field lines, which stretch out from the central compact object, make up the jet. They turn around at the tip of the jet (which is located outside of Figure 3 frame) and return back in a layer that surrounds the jet. The returning field lines carry no energy flux and they make up an *inner magnetised cocoon* that separates the magnetic jet from the funnel wall. The jet and the inner cocoon are separated by a surface at which the poloidal field lines switch direction and b_p has a local minimum, leading to a peak in the value of b_ϕ/b_p . This surface marks the jet outer boundary and is located in Figure 3(c) at $R_j \simeq 15$. The ratio b_ϕ/b_p is close to unity in the jet and the Lorentz factor increases from the jet axis toward the jet edge. Figure 4 shows the profiles of b_ϕ , b_p and $\gamma\beta$ across the jet at the height $z = 200$. The strong b_p with a comparable strength to b_ϕ outside the light cylinder ($R > 1$) is clearly seen. Also evident is the flat profile of both field components, in agreement with eqn. (11), (12), and the linear growth of $\gamma\beta$ which is expected in such a case (eq. 8). The combination of a flat magnetic field profile with a dominant poloidal component, together with the high Lorentz factors renders headless jets stable to kink instability.

5 AXIALLY SYMMETRIC HEADED JETS: JETS MOVING THROUGH A DENSE MEDIUM

Magnetised jets propagating in a dense stellar envelope need to drill a hole through the star before they can emerge from it. Such jets are substantially different than the *headless* jets that propagate in a previously evacuated funnel and that we discussed in Sec. 4. When a jet propagates through a dense external medium at a speed that exceeds the ambient sound speed, it pushes the ambient gas in front of it, forming a bow shock, as illustrated in Fig. 1(a) with the solid blue line. The ambient gas that crosses the shock heats up and forms a cocoon around the jet (shown in green in Fig. 1). The cocoon applies pressure on the jet and collimates it, thus playing the role of the confining walls in the previous example. In this case, however the jet continuously expends energy on drilling the hole and pushing the ambient gas sideways. This causes the jet to slow down mainly at its upper part, or the *jet head* (shown in dark blue in Fig. 1), where most of the work is being made.

The basic features of the jet, the bow shock and the cocoon are seen in Fig. 5 that shows a meridional slice of the density (left panel) and the pressure (right panel) in a 2D simulation of the jet. The shock is seen as a sharp jump in colour in the density (left) and pressure (right) panels. To simulate the jet we used a similar setup as in the headless jet case: a rotating sphere with a monopole field that is placed at the center of the grid and is surrounded by a cold ambient medium. However here the medium completely surrounds the sphere and follows a power-law density (see Table 1, model M2). As in the previous case the presence of the ambient medium causes the poloidal field lines to collimate along the rotational axis. The poloidal field lines, shown with black lines, extend from the jet base at the central object out to the jet head, at which they turn around and return back. Similar to the headless jet case, they form an inner magnetised cocoon that shields the magnetic jet from the non-magnetic cocoon of the shocked ambient gas. The outgoing magnetic flux, which makes up the jet, has an elongated, nearly cylindrical ‘cigar’ shape: its radius at the widest point is $R_j \simeq 30$.

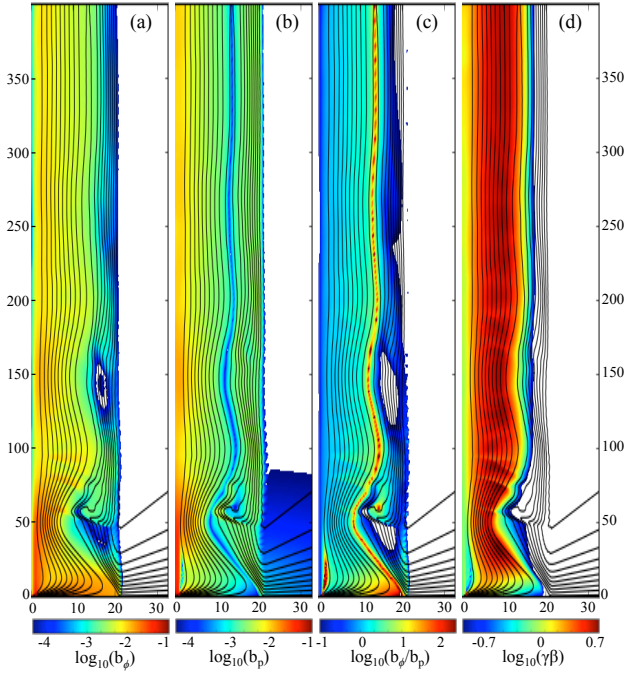


Figure 3. The 4 panels show, from left to right, the values of b_ϕ , b_p , b_ϕ/b_p and $\gamma\beta$ in a headless 2D jet. The unit of length is the light cylinder radius, $R_L = 1$. The jet propagates inside of a preexisting low-density cylindrical funnel (of radius $R = 20R_L$) carved out in a high-density ambient medium. The central object produces an equatorial outflow, which bounces off the funnel walls and re-collimates at $z \sim 10$, forming a pair of jets (we show only one of them). After several oscillations, the cylindrical radius of the jet settles to $R_j \sim 13$. The jet is surrounded by returning magnetic field lines, which fill the rest of the cavity but carry very little to no energy flux, as indicated in the leftmost panel by the low value of b_ϕ there. The two middle panels show that in the jet the toroidal and poloidal magnetic field components are roughly in equipartition in the fluid frame, $b_\phi \lesssim b_p$. The rightmost panel shows that the jet Lorentz factor is largest at the edge of the jet, as expected from the analytic models (see Sec. 4). See Fig. 4 for the transverse profiles of quantities shown in this figure. Since the ambient density is extends out to infinity and the walls are rigid, the headless jet eventually reaches a steady state. See Figs. 5–7 to compare to headed jets that do not have a pre-existing funnel to propagate through and have to drill one themselves.

The velocity of the jet head, $\beta_h \simeq 0.5$, is substantially lower than the velocity of the jet material which is practically c , at the time shown in Fig. 5, as we discuss below.

To support the propagation of the jet head, the pressure in the jet increases, mainly due to the increase in the toroidal field strength. Another way to look at this is that the slower moving head blocks the free expansion of toroidal field which otherwise would stream upward with a super-fast magnetosonic velocity obtained in eq. (8). Since toroidal field keeps getting injected into the jet by the winding of the field lines at the bottom of the jet, the toroidal field accumulates in the jet, and the ratio of toroidal to poloidal field increases.

The jet and the cocoon are in pressure balance, and the width of the jet is determined by the pressure profile of the cocoon along the jet-cocoon boundary. This profile is relatively flat in the longitudinal direction, leading to the near-cylindrical cigar-like jet shape seen in Fig. 5. Moreover, the cocoon expands sideways with a velocity that is much slower than the velocity of the jet material along the jet. Thus, the typical timescale for the cocoon pressure to drop

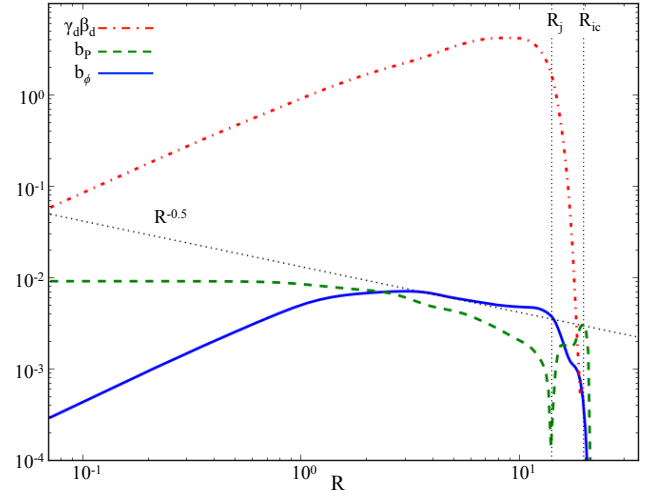


Figure 4. The cross-sectional profiles of the drift 4-velocity (dash-dotted red), b_p (dashed green) and b_ϕ (solid blue) in a headless jet (model M2Cyl), taken at an altitude $z = 200R_L \sim 2 \times 10^9$ cm. The fluid-frame toroidal magnetic field increases inside the light cylinder, $R_L = 1$, peaks just outside of it and then drops off as $b_\phi \propto R^{-1/2}$. The profile of b_p is flat inside and slowly decreases outside of the light cylinder until the jet edge at $R_j = 13R_L$. The sharp decrease in b_p at R_j occurs due to the flip in the direction of the field lines at the edge of the jet, marked by R_j . The returning field lines fill the rest of the cavity up to $R_{ic} = 20R_L$ and form an inner cocoon that separates the jet from the medium outside the funnel. The poloidal and toroidal magnetic field components are roughly in equipartition inside the jet, $b_p \simeq b_\phi$. As a result (see eq. 8), the drift velocity $\gamma_d\beta_d$ scales linearly with R , and reaches a peak value of $\gamma_d\beta_d = 5$ at $R = 7R_L$. The full morphology of the jet is shown in Fig. 3.

by a factor of two is much longer than the timescale for a jet fluid element to double its height. This implies that instantaneously we can approximate the jet geometry as a steady-state cylindrical jet, and we can use the force-balance equation (9) to analyse the transverse profile of the magnetic field in the jet.

Here again we need to know the relationship between b_ϕ and b_p . Due to the accumulation of toroidal field in the jet, we approximate $b_\phi \gg b_p$ at $R \gg R_L$, which leads to the following solution to eq. (9):

$$b_\phi \propto \begin{cases} R & , R \ll R_L \\ R^{-1} & , R \gg R_L \end{cases} \quad (13)$$

The excess of toroidal over poloidal field implies that the acceleration of the plasma cannot be very efficient. Substituting the approximation $b_\phi \gg b_p$ in eq. (7), we get that the drift 4-velocity is now

$$\gamma\beta_j \approx \frac{E}{(B_\phi^2 - E^2)^{1/2}} \simeq 1, \quad (\text{headed jets}) \quad (14)$$

where we assume here that $|B_\phi|$ exceeds E by an order unity factor due to the accumulation of toroidal field. In this case eq. (6) which is still correct in the lab frame, holds approximately for the fluid-frame as well, namely $b_p \simeq b_\phi R_L/R$. This implies that

$$b_p \propto \begin{cases} \text{constant} & , R \ll R_L \\ R^{-2} & , R \gg R_L \end{cases} \quad (15)$$

Comparison with eq. (11) shows that the profiles of both components of the magnetic field in this case are steeper at $R > R_L$ than in the case of a headless jet.

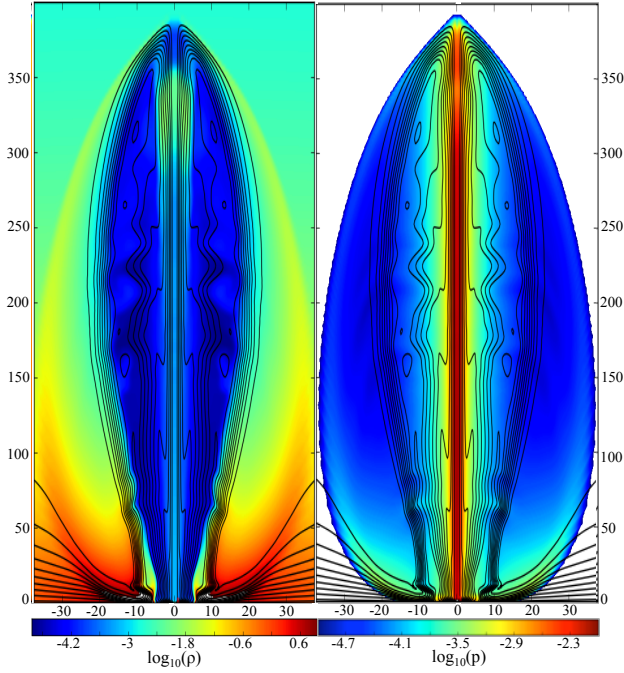


Figure 5. Meridional slices through a 2D *headed* jet, i.e., a jet that propagates through a dense ambient medium (without any pre-drilled funnel), at a time $t = 730R_L/c \sim 0.25$ s in the fiducial 2D model M2. Density (left panel) and pressure (right panel) distributions are shown in colour on a log scale (see the colour bars). Solid black lines show magnetic field lines, which extend from the surface of the central compact object out to the jet head and return back on the outside of the jet. Because the jet head moves supersonically relative to the ambient sound speed, an arrowhead-shaped bow shock forms and appears as a sharp jump in colour in both panels. The ambient gas, which is heated at the shock, forms a *cocoon* that pressure supports the jet and causes it to assume a cigar-like shape. The bow shock expands sideways with time, and the cocoon pressure decreases. As a result the jet slowly widens and never reaches a true steady state (compare to headless jets in Fig. 3).

To illustrate the magnetic field properties and the dynamics in the headed jets, we show in Fig. 6(a)–(d) the spatial distributions of b_ϕ , b_p , b_ϕ/b_p , and $\gamma\beta$ of the jet shown in Fig. 5. The colour bars are the same as in Fig. 3, to allow for easy comparison to the headless jets. Panel by panel comparison of Fig. 6 and Fig. 3 shows that in headed jets b_ϕ is stronger (panel a) and b_p is much more concentrated toward the axis (panel b) in the headed jet, as expected from our analytic scalings of the field profiles (see eqs. 11–15). Therefore b_ϕ/b_p (panel c) is much higher in the headed jet than in the headless jet. The two red stripes that appear at $R \approx 5$ and $R \approx 15$ mark regions where the poloidal field flips direction. The 4-velocity (panel d) is much lower in the headed jet than in the headless jet, as expected due to the need for the headed jet to drill through the ambient medium.

Figure 7 shows the jet properties in a more quantitative way by plotting the 1D profiles of b_p , b_ϕ and the drift 4-velocity $\gamma_d\beta_d$ across the jet. The profiles are measured at $z = 200R_L \sim 2 \times 10^9$ cm, the widest point of the headed jet where it has a similar width to the headless jet and a geometry that is close to cylindrical, making it easy to compare the two cases (see Figs. 5–6). It can be seen that b_ϕ peaks at $R \sim R_L$ and scales as $b_\phi \propto R^{-1}$ beyond that, in agreement with eq. (13). This profile is steeper than for the headless jet, $b_\phi \propto R^{-1/2}$, as seen in Fig. 4. On the other hand, b_p has a flat

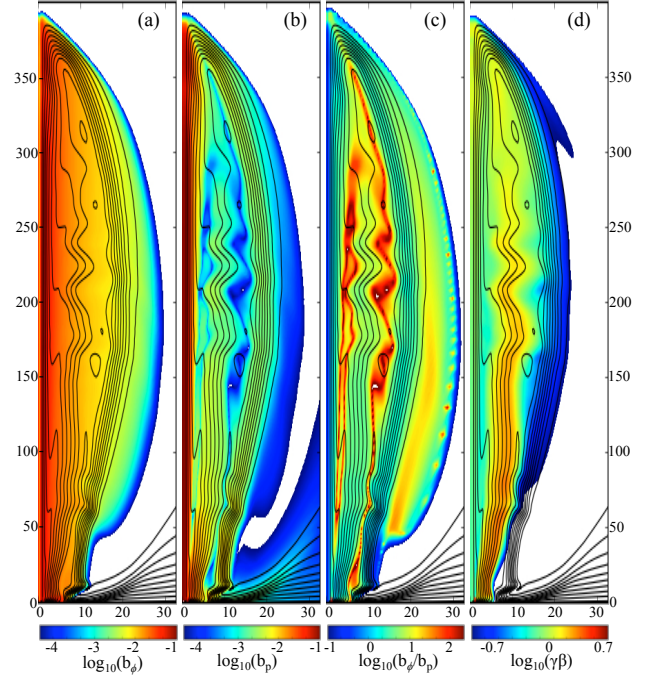


Figure 6. The 4 panels show, from left to right, meridional slices of b_ϕ , b_p , b_ϕ/b_p and $\gamma\beta$ of a headed jet drilling its way through a dense ambient medium, at a time $t = 730R_L/c \sim 0.25$ s in our fiducial 2D model M2. The colour scheme is the same as for the headless jet in Fig. 3 for ease of comparison. Poloidal field lines are shown as black solid lines. The edge of the jet, the boundary between outgoing and returning field lines, is located at $R_j \approx 10\text{--}15R_L$. Along the jet edge the poloidal field reaches a minimum and the ratio b_ϕ/b_p reaches a maximum (panel c). See Fig. 7 for profiles of various quantities across the jet.

core at $R < R_L$ and drops sharply outside of it to a very low value, $b_p \ll b_\phi$, unlike in the headless case for which $b_p \approx b_\phi$. As a result, the acceleration is much less efficient in headed jets, with $\gamma_d\beta_d \lesssim 2$ across the jet. The combination of these three properties – higher b_ϕ/b_p ratio, steep profile of b_p , and lower $\gamma\beta$, suggests that headed jets are unstable to kink modes. As we show in the next section, this leads to jets that are very different than the headless jets.

6 KINK MODES IN HEADED POYNTING-DOMINATED JETS

Kink instability is a 3D effect and cannot be studied with axially-symmetric simulations. It develops in regions that are dominated by the toroidal field (in the proper frame) and that maintain strong causal connection across the jet (eq. 4). For this reason, collimated jets are ideal environments for the development of the kink instability. Here we show that the instability evolves in two stages. First, it grows internally in the jet without affecting the overall jet morphology. This instability is often referred to as the *internal kink*. It converts the magnetic energy into thermal energy via magnetic reconnection. As a result, the toroidal magnetic field decays, and the jet finds itself in a stable configuration that inhibits further growth of the internal kink. However, kink modes can still grow externally on the periphery of the jet and perturb the entire jet body. Such an *external kink* instability grows over longer time scales and typically affects the outer parts of the jet, near the jet head. As we will see below, as a result of the external kink, the jet head wobbles and in-

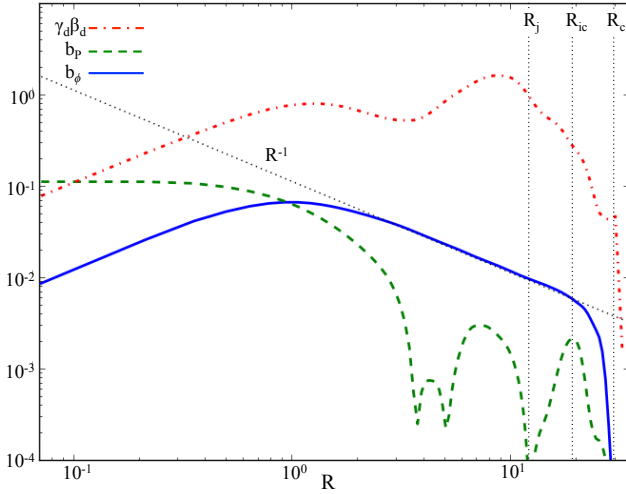


Figure 7. The cross-sectional profiles of the drift 4-velocity (dash-dotted red) and the two fluid-frame magnetic field components, b_p (dashed green) and b_ϕ (solid blue), in a headed 2D jet (model M2) at an altitude $|z| = 200R_L \sim 2 \times 10^9$ cm. Here, the fluid-frame magnetic field scales as $b_\phi \propto R^{-1}$ and peaks around the light cylinder, $R_L = 1$. The profile of b_p is flat inside and drops sharply at $R \gg R_L$, where the toroidal field dominates, $b_\phi \gg b_p$. As a result, the drift velocity $\gamma_d \beta_d$ remains of order unity across most of the jet. This is in contrast to the headless jet that accelerates to much higher velocities (see Fig. 4). The radii of the jet, which contains the outgoing magnetic field lines (R_j), the inner cocoon, which contains the returning field lines (R_{ic}), and the outer cocoon, which is made up of shocked ambient gas (R_c), are marked with dotted vertical lines. The full morphology of the headed jets is shown in Figs. 5–6.

creases its effective cross-section. This makes it harder for the jet to drill its way through the ambient medium and decreases the jet propagation velocity.

6.1 The growth of internal kink in a collimated headed jet

An outflow from the central compact object is initially over-pressured relative to the surrounding medium and expands in all directions. As the flow expands, its pressure drops until it becomes comparable to the surrounding pressure of the confining medium, and the outflow becomes collimated.

Before the collimation point, the jet internal pressure exceeds the pressure of the cocoon, so the jet material expands freely. The Lorentz factor scales as $\gamma_j \propto R/R_L$ (eq. 8) until $\gamma_j = \theta^{-1}$. From this point on, the jet material loses the strong causal contact with the jet axis and the acceleration continues less efficiently (Tchekhovskoy et al. 2008). During the free expansion phase kink modes cannot grow, since their typical growth time is longer than the propagation time. Indeed, from eq. (2), it follows that in the linear acceleration regime $t_{\text{kink}} \approx 2\pi R^2/R_L c > R/c \sim t$. Beyond that the loss of strong causal contact inhibits the growth of the kink instability.

At the collimation point, the jet pressure becomes equal to the pressure in the cocoon. The conditions for strong causal contact are remet and the kink instability can grow. If the collimation takes place outside of the linear acceleration regime, then at the collimation point we have $b_\phi > b_p$. The hoop stress, which becomes effective and is proportional to b_ϕ^2 (see eq. 9), cannot be counterbalanced by the poloidal pressure. This leads to a recollimation point—contraction of the jet cross section—followed by a bounce when the poloidal pressure becomes strong enough to re-

sist the hoop stress, resulting in a nozzle-like shape (Lyubarsky 2009). In a headless jet its cylindrical radius continues to oscillate above the nozzle until the magnetic field configuration relaxes to an equilibrium state, described by eq. (10), and seen in Fig. 3. Since $b_\phi \simeq b_p$, this state is stable against internal kink modes (Lyubarsky 2009, 2011). In a headed jet, as Fig. 6 shows, these two components are not in equilibrium with each other, and the magnetic field continues to be dominated by b_ϕ above the collimation point (at $R \geq R_L$). This suggests that the jet can be unstable to the internal kink instability.

To check this we carried out 3D simulations whose setup is similar to that of our 2D simulations, with a few exceptions, as described in Sec. 2.2.³ For our fiducial model, M3, we use an ambient density that corresponds to a GRB jet with a luminosity 5×10^{49} erg/s propagating in a $10M_\odot$ star (see Tabs. 1 and 2 for a full list of models). Figure 8 shows a volume rendering of the inner regions of a headed jet in our fiducial model M3. The left panel shows in colour the quantity $\log_{10}(|\nabla \times \mathbf{B}|)$, which is a proxy for the conduction current density. The right panel shows the logarithm of magnetisation, defined here as $\sigma = B^2/4\pi w$. The light blue lines trace out the magnetic field in the lab frame (\mathbf{B}). Close to their footpoints, at $z \approx 0$, the field lines expand and have an ordered, toroidally-dominated configuration. The field lines are recollimated at $z \approx 20R_L \approx 2 \times 10^8$ cm and converge to the jet axis and rebound, forming a nozzle-like shape. As they approach the nozzle, they begin to kink and lose their ordered shape. This is accompanied with a drop in the σ parameter and a peak in the conduction current density, indicative of magnetic dissipation. The helical pattern of the dissipation region is characteristic of the kink instability. Above the dissipation region the field lines are less twisted and have a stronger poloidal component, which points to a dissipation that affects mostly the toroidal magnetic field component.

Not all field lines lose the strong causal contact with the axis in the free expansion region. If the jet is collimated at an altitude z_{coll} then strong causality is maintained across the field lines with an opening angle $\theta < \sqrt{R_L/z_{\text{coll}}}$ up to z_{coll} . If, in addition, the Lorentz factor along the field lines is not too high, $\gamma_j < \sigma_0^{1/3}$, the flow remains sub-fast magnetosonic. In this case it can “feel” the decelerating material at the recollimation nozzle, above it. This has a similar effect as the slower moving head and leads to an increase in the toroidal field strength: toroidal field accumulates, the acceleration becomes inefficient, and the region becomes kink unstable. The two conditions are met along field lines with an opening angle satisfying

$$\theta < \theta_k = \begin{cases} \sqrt{\frac{R_L}{z_{\text{coll}}}} & , z_{\text{coll}} < R_L \sigma_0^{2/3}, \\ \frac{R_L}{z_{\text{coll}}} \sigma_0^{1/3} & , z_{\text{coll}} \geq R_L \sigma_0^{2/3}, \end{cases} \quad (16)$$

and render the field lines kink unstable below the recollimation nozzle.

To study this effect in more detail and to better capture the small-scale structure of the dissipation region, we reran our fiducial 3D model M3 at twice the resolution in each dimension. We

³ In 3D simulations, the rotational axis is directed not along the z -axis, as in 2D ones, but along the x -axis, to avoid the interaction of the jets with the coordinate singularity. Accordingly, the radial 3D grid lines collimate toward the x -axis. For simplicity of presentation, in the text we will still use the standard axis orientation, with the z -axis pointing along the rotational axis.

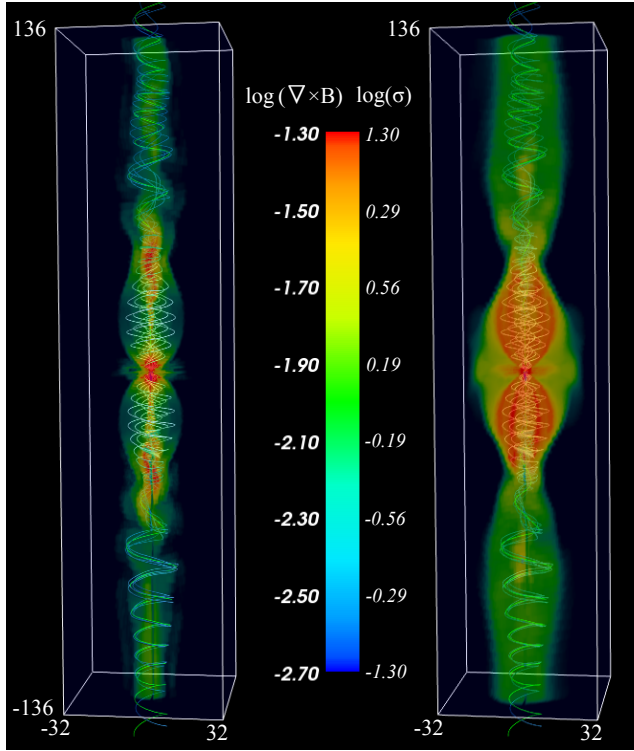


Figure 8. A snapshot of the central region in our fiducial 3D model M3 at $t = 4400R_L/c \sim 1.5$ s, when the jet head is at $z = 1000R_L \sim 10^{10}$ cm, or about 10% of the stellar radius. The colour scheme in the left panel shows the $\log_{10}(\nabla \times \mathbf{B})$, which is a tracer of conduction currents, and the right panel shows the $\log_{10}(\sigma)$, which is a tracer of magnetisation. The solid lines show the field lines of \mathbf{b} , the magnetic field as measured in the fluid frame and traced out in the lab frame. The degree of their twist reflects the degree to which the toroidal magnetic field component dominates in the fluid frame. The jet is initially freely expanding sideways out to $|z| \approx 30R_L$ where it recollimates due to the confining pressure of the cocoon. The free expansion region is characterised by a low current density (green colour) and a high σ (red colour; see the colour bar). Above this region, σ approaches unity (green colour) and the field lines become less toroidally twisted. Both of these reflect the dissipation of the toroidal magnetic field into heat above the collimation point. There the magnetic field lines converge to the axis and become unstable to the internal kink mode, which is seen as a helical pattern in the jet (see Sec. 6.1).

refer to this high-resolution simulation as model M3HR (see Table 1). Figures 9 and 10, show the longitudinal cross-sections of the jet along the $y-z$ plane (left panel) and the $x-z$ plane (right panel) in this high-resolution model. The jet propagates along the z -axis. The colour schemes are the same as in the corresponding 3D jets in Fig. 8. Regions where magnetic energy is dissipated are identified by a decrease in the σ parameter accompanied by the high conduction current. Below the nozzle there is a cone of an opening angle $0.1 \leq \theta \leq 0.17$, which is kink unstable all the way down to the source. The jet becomes collimated at $z_{\text{coll}} \approx 17$ (see Fig. 10), the opening angle of the unstable cone is in agreement with eq. (16) for our choice of the initial jet magnetisation of $\sigma_0 = 25$ (see Sec. 2).

Most of the magnetic energy dissipation occurs at the collimation nozzle and above it. In this region magnetic field lines with different pitch angles converge and become kink unstable. The dissipation process that follows leads to the straightening of the field lines, by reconnecting out the local toroidal component and results in a gradual alignment of the field lines with the helical path of

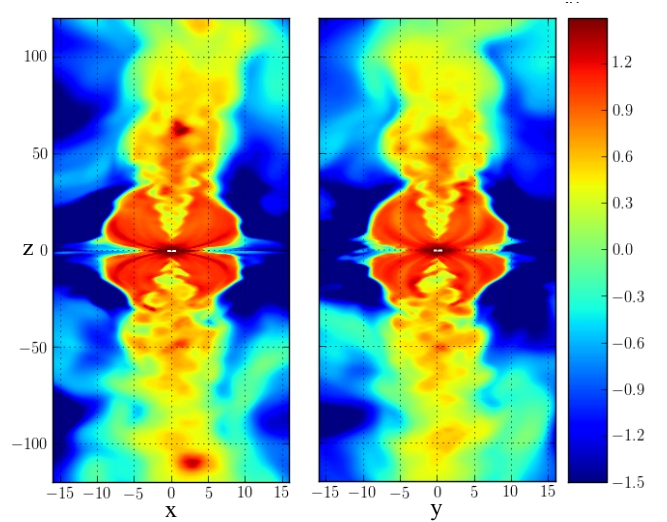


Figure 9. Meridional slices of $\log_{10}(\sigma)$ through the $x-z$ (left) and $y-z$ (right) planes, in a 3D jet at time $t = 2984R_L/c \approx 1$ s in our high-resolution 3D simulation, model M3HR. Note that the horizontal axis scale has been stretched by approximately an order of magnitude to clearly show the jet structure. The jets start out highly magnetised, with $\sigma_0 \approx 25$. They recollimate at $z_{\text{coll}} \approx 17R_L \approx 1.7 \times 10^8$ cm, converge onto the axis, and develop an internal kink instability, which is seen as small-scale yellow-red wiggles in the jets. The decrease of the magnetisation (seen as the transition in colour from red to yellow) at the wiggles reflects magnetic energy dissipation via the internal kink instability. Some field lines, which have small enough opening angles to maintain strong causal contact across the jets, become unstable earlier and dissipate their energy at lower altitudes. These lines form a ‘wedge’ of lower σ that extends down to $|z| \approx 10R_L \approx 10^8$ cm.

the jet axis. An example for such small angle reconnection can be seen in Figure 11. It shows a closeup of the field lines at the collimation point, where most of the reconnection occurs. We trace out several magnetic field lines starting out with polar angles of $\theta = 0^\circ, 20^\circ, 30^\circ, 50^\circ, 70^\circ$ on the rotating sphere. The left panel of Fig. 11 shows the field lines in an unconventional sense: it shows the field lines of *proper frame magnetic field*, \mathbf{b} , that are traced out in the lab frame. These field lines are useful for determining the regions that are prone to becoming kink-unstable: this is because the growth of the kink instability depends on the ratio b_ϕ/b_p , which is seen in the figure as the degree of azimuthal winding of the field lines. These field lines also give an idea of the proper angle between two reconnecting field lines at the reconnection point. The right panel of Fig. 11 shows the conventional lab-frame field lines \mathbf{B} . From the comparison of the two panels, we see that the proper field lines appear to be more disordered than the lab frame ones, and this can be a factor in encouraging their rapid reconnection. The volume rendering colour scheme shows the logarithm of the magnetisation, $\log_{10} \sigma$. The high- σ jet appears as a dark silhouette against the blue low- σ background. The colour of the field lines represents $\log_{10} h$, where $h = w/\rho$ is the specific enthalpy. Regions where the field lines are turning red are the regions where the dissipation is taking place. The green line in each of the two panels indicates the polar field line, which starts at the north pole of the magnetar and follows the centre of the jet. As expected from the causality condition (16) and seen in Fig. 11, the green line begins to kink even before the jet converges onto the jet axis. The field lines with larger opening angles begin to kink only after the flow converges onto the axis. These outer field lines are initially strongly

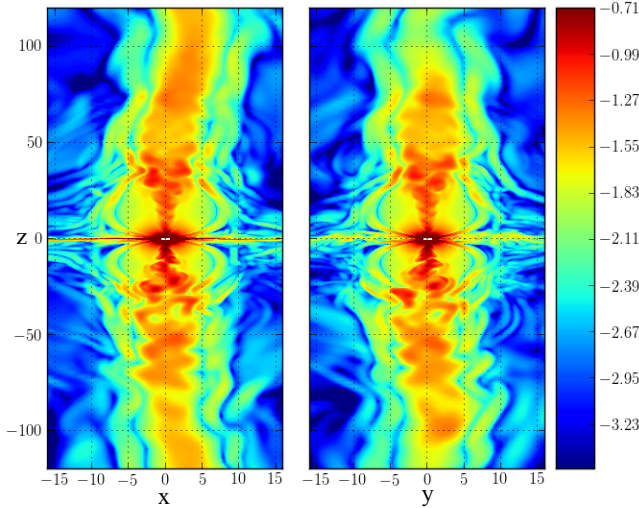


Figure 10. Same as Fig. 9 but for meridional slices of the conduction current $J \propto \log_{10}(|\nabla \times \mathbf{B}|)$. High (red) values of J indicate regions with particularly strong magnetic field twist and particularly strong dissipation.

twisted around the central, green field line. However, as they dissipate their magnetic energy into heat, they gradually straighten out and become aligned with the green line (as seen in Fig. 11).

6.2 External kink above the dissipation region

The dissipation of magnetic field above the collimation point leads to two important outcomes. First, it relieves some of the toroidal pressure and decreases the ratio of b_ϕ/b_p in the jet. As a result, R_0 , the radius of the poloidal field dominated core, which controls the minimal growth time of the kink instability (see eq. 2), increases significantly. This process is depicted in Fig. 12 which shows $\log_{10}(|b_p/b_\phi|)$ in a cross section cut along the jet: the core starts out as a narrow spine at the base of the jet and gradually widens above the collimation point, at which most of the dissipation occurs. Second, the dissipation generates thermal energy at the expense of toroidal magnetic field energy. In the presence of the thermal pressure, the transverse magnetic field profile flattens out. As we discussed in Sec. 3, both of these changes stabilise the jet against the further growth of kink modes at the jet inlet. In fact, we see that the internal kink saturates and the dissipation stops when the equipartition is reached between the thermal pressure and the magnetic pressure.

To demonstrate the effect of the thermal pressure on the configuration of toroidal field, we return to the force balance equation (eq. 9) and include a thermal pressure term. In a cylindrical jet, the equation takes the form,

$$\frac{db^2}{8\pi dR} + \frac{b_\phi^2}{4\pi R} + \frac{dp_{\text{th}}}{dR} = 0, \quad (17)$$

where we neglect here the poloidal hoop stress term. We assume an approximate equipartition between the thermal and magnetic pressures, i.e. $p_{\text{th}} = b^2/8\pi$. The solution to eq. (17) inside the core where $b_\phi \ll b_p$, is $b_p = \text{const}$. The resultant profile of b_ϕ is

$$b_\phi \propto \begin{cases} R & , R < R_0, \\ R^{-1/2} & , R > R_0. \end{cases} \quad (18)$$

This profile is similar to that of the headless jet (eqs. 11 and 12); the

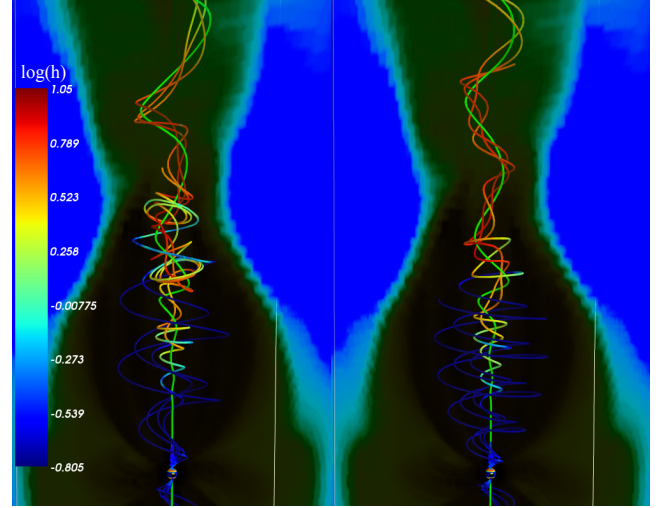


Figure 11. A zoom-in on the jet recollimation nozzle that is seen in Fig. 8 at $z \sim 50R_L \approx 5 \times 10^8$ cm (model M3 at $t = 4400R_L/c \sim 1.5$ s). The left panel shows field lines in the fluid-frame \mathbf{b} as traced out in the lab frame. This unconventional representation of the magnetic field lines is useful for visually determining the degree of toroidal dominance of the magnetic field in the fluid-frame (see the text for details). The right panel shows the conventional field lines of the lab-frame magnetic field, \mathbf{B} . The fluid-frame magnetic field lines are more disordered, which might reflect their readiness to reconnect and dissipate their energy. We show the field lines that originate at the surface of the magnetar with polar angles at their foot points equal to 0° , 20° , 30° , 50° , and 70° . The colour scheme represents $\log_{10} h$ on the field lines, where h is the specific enthalpy. The volume colour rendering represents $\log_{10} \sigma$. The jet has a higher σ than the confining cocoon and appears as a dark silhouette against the blue background. The field line, which originates at the north pole of the magnetar, indicates the jet axis and is shown in green. The gradual straightening of the magnetic field lines along the green line is clearly seen in both panels and reflects the dissipation of the toroidal magnetic field due to the internal kink instability.

only difference here is that outside the core, $R > R_0$, the high thermal pressure replaces b_p and flattens out the transverse profile of the toroidal field. Figure 13 shows the magnetic and thermal pressure profiles across the simulated jet, above the dissipation region. The profiles are measured in a snapshot of a jet in the model M3, at a time $t = 4400R_L/c \approx 1.5$ s (same as in Fig. 8) and an altitude $z = 400R_L \approx 4 \times 10^9$ cm, which is well above the region where most of the dissipation takes place. We average the profiles in the azimuthal direction to smooth out the small axial asymmetries due to the external kink modes. We show the azimuthally averaged $\langle b_\phi \rangle$ (solid blue), $\langle b_p \rangle$ (dashed green), $\langle b \rangle$ (solid grey) and $\langle \sqrt{8\pi p_{\text{th}}} \rangle$ (dash-dotted red). As expected from eq. (18), the magnetic field configuration is split into two regions: i) an inner core, dominated by poloidal field with a flat profile that extends to $R_0 \approx 10$, ii) an outer region, dominated by toroidal field with a profile $b_\phi \propto R^{-1/2}$ that covers the outer jet, at $R_0 \leq R \leq R_j \approx 36R_L \approx 3.6 \times 10^8$ cm, and extending into the inner cocoon, $R_j < R \leq R_{\text{ic}} \approx 60 \approx 6 \times 10^8$ cm. Within the jet, magnetic and thermal energies are indeed in equipartition, which is the assumption under which we obtained the scaling (18).

The combination of a flat magnetic field profile and a high thermal pressure stabilises the jet. Mizuno et al. (2012) found that kink instability is suppressed in jets with toroidal field profiles as shallow as $\propto R^{-1/2}$, while Mignone et al. (2010) reached a similar conclusion when they tested the stability of hot magnetised jets.

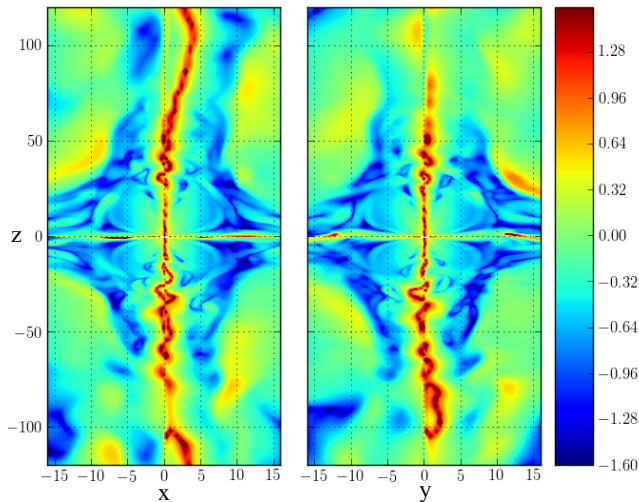


Figure 12. Similar to Figures 9 and 10 but for meridional slices of $\log_{10}(b_p/b_\phi)$. Dark red colour shows the poloidally-dominated regions and their transverse extent reflects the value of R_0 , the cylindrical radius of the jet core with $b_p \gg b_\phi$. We see that above the collimation point, $|z| \gtrsim 30R_L$, the value of R_0 increases with increasing distance away from the central compact object. This increase reflects the conversion of the toroidal magnetic field into heat by the internal kink mode. Notice that the top jet in the right panel moves off the image plane due to the external kink.

Thus, above the dissipation region the hot jet material is stable to the internal kink modes and is expected to behave in a similar way to a hot, purely hydrodynamic flow. However, we find that kink instability can still grow around the jet perimeter. This is known as the *external kink* mode, which produces helical motions that deform the entire body of the jet. This is seen in Fig. 14 as the large-scale bends of the (blue) jets. External kink grows on a time scale of the order of the time it takes an Alfvén wave to travel around the jet perimeter. Typically it takes $\sim 5 - 10$ growth times for the global kink modes to grow substantially, and this is why most of the deformation occurs at the top, “older” parts of the jet, mainly near the jet head where the kink instability has the longest time to evolve. The helical motions of the kink-unstable head increase the effective cross-section of the jet and reduce its propagation velocity. If the external kink grows to a high enough amplitude, it can even disrupt the jet and cause it to stall.

6.3 Dissipation rates and convergence tests

One of the important results of this work is the efficient dissipation of the magnetic field at and above the recollimation nozzle. This reduces the strength of the toroidal magnetic field component and leads to equipartition between thermal and magnetic energies. A similar transition in the magnetic field configuration was seen in the simulations of twisted magnetic flux tubes that underwent dissipation via the internal kink (e.g. Hood et al. 2009; Gordovskyy & Browning 2011; Pinto et al. 2015). Once started, the dissipation in our simulation occurs over a length scale of $\lesssim 10R_j$, which is consistent with the expected growth time of the kink instability across the entire jet (see e.g. Fig. 9). This rate is also consistent with the dissipation rate found in other simulations (e.g. Mizuno et al. 2012; Porth & Komissarov 2015).

To test the effect of the grid resolution on the dissipation rate, we reran our fiducial simulation, M3, with twice the resolution in

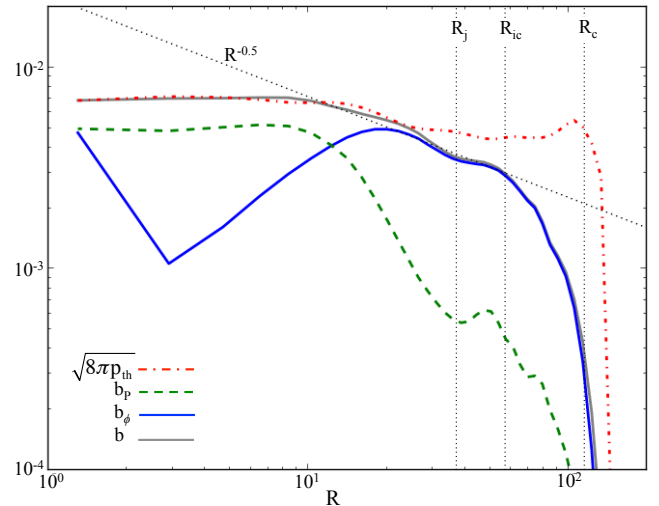


Figure 13. Transverse profiles of the magnetic field components and the thermal pressure in the jet shown in Fig. 8 (fiducial model M3), taken at an altitude $z = 400R_L \sim 4 \times 10^{19}$ cm, $t = 4400R_L/c \sim 1.5$ s, and averaged over the azimuthal direction to smooth out non-axisymmetric effects. We show $\langle b_\phi \rangle$ (solid blue), $\langle b_p \rangle$ (dashed green), $\langle b \rangle = \langle \sqrt{b_p^2 + b_\phi^2} \rangle$ (solid grey) and $\langle \sqrt{8\pi p_{th}} \rangle$ (dash-dotted red). Here, the poloidal and toroidal field components are defined with respect to the magnetar’s rotational axis, and the actual jet axis might deviate from it due to the external kink mode. The magnetic field profile consists of a core of radius $R_0 \sim 10R_L \approx 10^8$ cm, which is filled with a nearly uniform poloidal magnetic field, and is surrounded by a sheath, which is dominated by a toroidal field of a transverse profile, $b_\phi \propto R^{-1/2}$. The toroidal field dominated region covers the outer parts of the jet ($10R_L \lesssim R \lesssim R_j \approx 36R_L \approx 3.6 \times 10^8$ cm) and the inner cocoon ($R_j \lesssim R \lesssim R_{ic} \approx 60R_L \approx 6 \times 10^8$ cm). The outer cocoon, which contains the shocked ambient matter and is dominated by thermal pressure, covers the region $R_{ic} \lesssim R \lesssim R_c \approx 120R_L \approx 1.2 \times 10^9$ cm.

each direction. We refer to this high-resolution simulation as model M3HR (see Table 1). Figure 15 shows the electromagnetic energy flux (dashed lines) and the thermal energy flux (solid lines) in the fiducial model M3 (blue) and its high-resolution version, model M3HR (green). For a proper comparison, the jets are taken to have the same z_h . Because in the high resolution simulation the jets propagate at a velocity that is somewhat slower (by $\sim 25\%$) than in our fiducial resolution simulation, the snapshots are taken at slightly different times. Even though the propagation velocities are different, the dissipation rates are similar. Moreover, the jet width in both cases is $R_j \approx 10R_L \approx 10^8$ cm and the dissipation occurs over a range $\Delta z \lesssim 100R_L \approx 10^9$ cm that agrees with the expected kink growth timescale at this distance. We have not tested how the dissipation rate depends on the Riemann solvers used in the code (see e.g. O’Neill et al. 2012); this will be studied elsewhere.

The $\sim 25\%$ difference in the head velocity comes from the fact that the high resolution jet is somewhat less stable to the external kink than the lower resolution jet, and the wobbling motions of the head have a somewhat larger radius. As we show in Sec. 7, the head velocity is inverse proportional to the head radius. Thus the wobbling motions increase the effective jet radius by $\sim 25\%$. Our simulations are therefore not fully converged in the context of the external kink and the head velocity, and it is desirable to make a proper convergence test. Such a test, however, is hard to carry out in global simulations like ours, due to the large computational resources required. An alternative is to perform a convergence test for the amplitude of the external kink instability in a small periodic

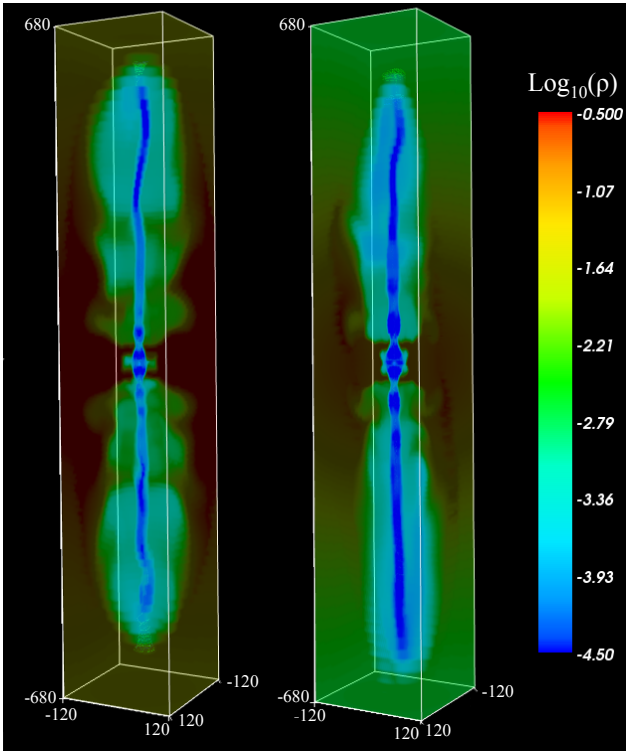


Figure 14. The morphology of the jets of different powers. The left panel shows a low-power jet in model M3LP at $t = 10995R_L/c \sim 3.7$ s. The right panel shows a high-power jet in model M3 at $t = 4084R_L/c \sim 1.36$ s. The high-power jet is 10 times more power than the lower-power jet and propagates approximately 2.7 times faster, and it reaches the same distance as the low-power jet in a shorter time. The large-scale bends of the jets are characteristic of the external kink instability. The low-power jet is thinner and becomes external-kink unstable at a smaller distance. As a result, kink modes grow to a larger amplitude and deform it more strongly than the high-power jet.

box. Mizuno et al. (2009) conducted such a test and concluded that when the jet is resolved by more than 20 cells across, the amplitude of the external kink is not sensitive to the resolution. In our case the fiducial resolution jet contains ~ 14 cells in the transverse direction at $z_h = 160R_L \approx 1.6 \times 10^9$ cm, where we make the comparison between the jets. In the high resolution jet the number of cells is twice as large. Thus it is likely that we are close to the full convergence.

To sum up, our results are rather insensitive to the numerical resolution, suggesting the possibility that the dissipation rate and the jet velocity are determined by the underlying instability and not the details of the numerical scheme. Whereas the quantitative understanding of the dissipation rate requires even higher resolution studies to probe the asymptotic scaling of the instability properties with resolution, the saturation of the instability at equipartition between thermal and magnetic energies is a robust, important result of this work.

7 AN ANALYTIC MODEL FOR A HOT MAGNETIC JET

In the previous sections, we saw that the jet material dissipates about half of its magnetic energy via the internal kink instability. The dissipation continues until equipartition is reached between thermal and magnetic energies. Since the jet is hot and has a rel-

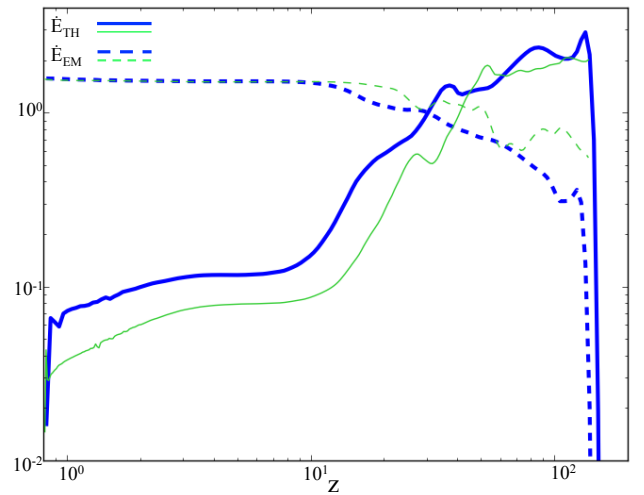


Figure 15. The thermal energy flux (solid lines) and the Poynting flux (dashed lines), as a function of z . We show the fiducial model, M3, at $t = 1885R_L/c \sim 0.6$ s (thick blue lines) and a high resolution model, M3HR, at $t = 2515R_L/c \sim 0.8$ s (thin green lines). Both jets extend to the same distance, $z_h \approx 150$, and have the same width, though the high resolution jet propagates at a velocity slower by 25% due to somewhat increased wobbling motions of the head. Even though the jets show some differences at their heads, the dissipation rates at their recollimation points are essentially the same. This indicates that the dissipation could be driven by a large-scale instability and not affected by the microphysics.

atively flat transverse pressure profile, it is stable to the internal kink modes (see Fig. 13 and Sec. 6.2). However, as Fig. 14 shows, that the jet (seen in dark blue colour) develops large-scale bends, characteristic of external kink modes. This means that, unlike hot hydrodynamic jets, hot magnetised jet can be unstable to the external kink mode. In the extreme cases, it is conceivable that the external kink could even lead to a complete disruption of the jet. In our simulations, we find that the external kink causes the head of the jet to wobble sideways, increasing the effective cross-section of the jet and decreasing its propagation speed.

Here, we investigate the conditions under which external kink modes can grow in the jet to a level where they affect jet propagation. Motivated by the fact that the jet is hot (see Sec. 6.2), we make use of its similarity to a hydrodynamic jet and employ an analytic model for the propagation of a hydrodynamic jet in a medium by Bromberg et al. (2011). We calculate the conditions in the jet and check if the external kink has sufficient time to grow and considerably deform the jet. A reader interested in the analytic results may skip directly to eq. (30), which gives the growth rate, and eq. (32), which estimates the propagation velocity of the jet.

Figure 16 illustrates our analytic jet model. We approximate the jet and the cocoon as concentric cylinders of the same height, z_h , and of radii R_j and R_c , respectively. We assume that the ambient medium is cold and has a power law density profile, $\rho_a \propto z^{-\alpha}$. Here and below, we use the indices j, h, c and a to describe quantities in the jet, the jet head, the cocoon and the ambient medium, respectively.

The jet and the cocoon are in pressure balance at their interface, $R = R_j$. We approximate the pressure in the cocoon as uniform, thus it can be evaluated as

$$p_c \approx \frac{E_c}{3V_c} \quad (19)$$

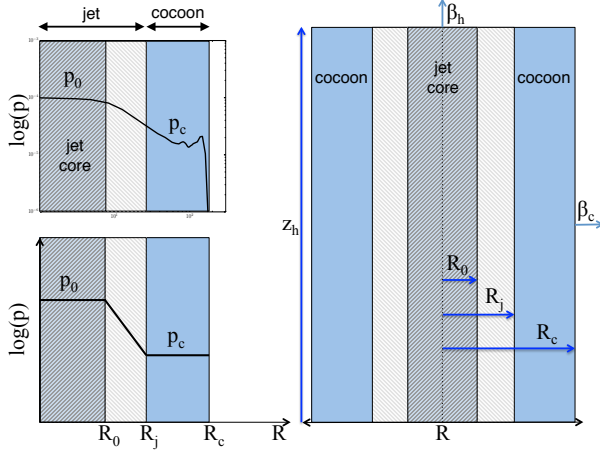


Figure 16. A schematic representation of our analytic jet model. Right panel: the jet (shown in grey) is composed of an inner poloidal–field–dominated core of radius R_0 , surrounded by a toroidal–field–dominated sheath of radius R_j . The jet is engulfed by a cocoon (light blue) of radius R_c . The jet head, located at $z = z_h$, propagates at the velocity $\beta_h c$ and the cocoon expands laterally at the velocity $\beta_c c$. Upper left panel: A lateral total pressure profile in a slice through the midpoint of a 2D jet in model M2 at time $t = 730R_L/c \simeq 2.4$ s. Lower left panel: an analytic approximation for the pressure profile. We assume a flat pressure profile in the jet core and the cocoon, and in the sheath we approximate the pressure as $p \propto R^{-1}$.

where E_c is the total energy in the cocoon, V_c is the cocoon volume, and we assume here a relativistic thermal equation of state.

The cocoon energy is injected at the jet head (see Sec. 5). Its value can be estimated as

$$E_c = \int L_j(\beta_j - \beta_h) dt, \quad (20)$$

where L_j is the jet luminosity, β_j and β_h are the velocities of the jet material and the head, respectively. The factor $(\beta_j - \beta_h)$ measures the reduction in the energy flux due to the motion of the head. The volume of the cocoon is estimated as

$$V_c \simeq \pi c^3 \int \beta_h dt \left(\int \beta_c dt \right)^2, \quad (21)$$

where $\beta_c = \sqrt{p_c/\rho_a c^2}$ is the sideways expansion velocity of the cocoon due to its own pressure. Combining eqs. (19), (20), and (21), and taking $t = \int dz_h/\beta_h c$ we obtain (up to an order unity numerical factor):

$$p_c \simeq \left(\frac{L_j^3 \rho_a}{\pi^3 z_h^4 R_j^4 c} \right)^{1/4}, \quad (22)$$

where ρ_a is evaluated at the jet head. A full calculation of the pressure is presented in Appendix A, where we follow the method of Bromberg et al. (2011).

Figure 16 shows a schematic plot of the pressure profile in the jet. Using the scaling given in Sec. 6.2 and eq. (18) we get:

$$p_j = \begin{cases} p_0 & , r \leq R_0, \\ p_0 \left(\frac{R_0}{R} \right) & , r > R_0, \end{cases} \quad (23)$$

where we take $R_0 \simeq R_j/2$ as the radius of the poloidal field dominated core. The jet pressure is connected to its luminosity via

$$L_j = 2\pi \int_0^{R_j} \frac{\Gamma}{\Gamma-1} p_j \gamma_j^2 \beta_j c R dR, \quad (24)$$

where Γ is the adiabatic index. An equipartition between the magnetic and thermal pressures results in $\Gamma = 3/2$ (See Appendix A). Substituting eq. (23) into eq. (24), we get the jet pressure at R_j :

$$p_j(R_j) \simeq \frac{2L_j}{9\pi\gamma_j^2\beta_j R_j^2 c} \quad (25)$$

We can now use eqs. (22) and (25) to solve for $\gamma_j R_j$ from the condition of pressure balance at the edge of the jet:

$$R_j \gamma_j \simeq \sqrt{\frac{2}{9\pi\beta_j}} \left(\frac{L_j z_h^4}{\rho_a c^3 \gamma_j^2} \right)^{1/6} \Psi \quad (26)$$

where $\Psi = [\pi(5-\alpha)(3-\alpha)/6]^{1/3}$ is an integration constant of order unity (see Appendix A).

External kinks grow in the jet on a time scale of the order of the Alfvén crossing time around the jet perimeter (eq. 2):

$$t_{\text{kink}} \simeq \frac{2\pi R_j \gamma_j}{v_A}, \quad (27)$$

where we made use of the fact that toroidal and poloidal fields are in equipartition at the jet edge. As we discussed above, typically it takes $\sim 5-10 \times t_{\text{kink}}$ for the instability to develop to a level where the jet is considerably deformed (Mizuno et al. 2012). The time available for the instability to grow is the time it takes a fluid element to reach the jet head:

$$t_{\text{dyn}} \simeq \frac{z_h}{c(\beta_j - \beta_h)} \simeq \frac{z_h}{c\beta_j}, \quad (28)$$

where we work in the limit where $\beta_h \ll \beta_j$. The jet will therefore be considerably kinked if

$$\frac{10\eta t_{\text{kink}}}{t_{\text{dyn}}} \simeq \frac{20\pi R_j \gamma_j \beta_j}{z_h} \lesssim 1, \quad (29)$$

where $0.5 \lesssim \eta \lesssim 1$, and we made use of the fact that the jet is highly magnetised, i.e., that $v_A \approx c$. Substituting $R_j \gamma_j$ from eq. (26) we get an expression for the stability of the jet to the external kink mode:

$$\Lambda \equiv \frac{10\eta t_{\text{kink}}}{t_h} \simeq 20 \sqrt{\frac{2\pi}{9}} \left(\frac{L_j}{\rho_a z_h^2 \gamma_j^2 c^3} \right)^{1/6} \frac{\sqrt{\beta_j}}{\beta_A} \eta \Psi \quad (30)$$

The propagation velocity of the jet is directly linked with the cross section of the jet head. In the limit where the head velocity is non-relativistic ($\gamma_h \beta_h \lesssim 1$), we can write (Matzner 2003; Bromberg et al. 2011):

$$\beta_h \simeq \sqrt{\frac{L_j}{\pi R_h^2 \rho_a c^3}}, \quad (31)$$

where R_h is the cross sectional radius of the jet head. As long as the helical motions of the head, due to the kink instability, are not large enough to increase the cross section of the jet substantially, we can use eq. (26) to estimate the velocity of the head:

$$\beta_h \simeq \sqrt{4.5\beta_j} \left(\frac{L_j \gamma_j^4}{z_h^2 \rho_a c^3} \right)^{1/3} \Psi^{-1} \quad (32)$$

Figure 17 shows β_h as a function of the location of the jet head in models M3 and M3LP, representing a GRB jet with a typical luminosity and with a low luminosity, respectively. We compare the values of β_h measured from the simulations, shown with thick solid lines, to the analytic values due to eq. (32), shown with thin dashed lines. Values for the high (low) luminosity jet are shown in blue (red). We also show the values of Λ from eq. (30) in dash-dotted lines. Both jets are marginally stable at small z_h (early times), and become increasingly more stable with time.

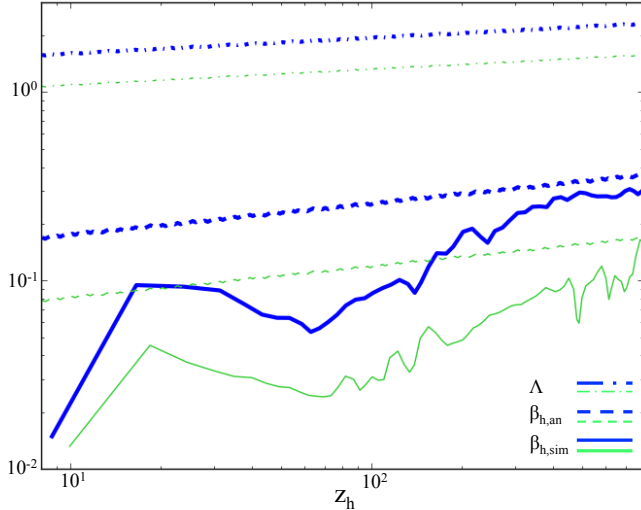


Figure 17. Jet head velocity β_h as a function of head position z_h for high-power (thick blue lines, model M3) and low-power (thin green lines, model M3LP) jets. The high-power jet is a factor 10 more luminous and propagates a factor of ~ 2 faster than the low-power one. We show the simulated values of β_h with solid lines, the analytic approximations according to eq. (32) with dashed lines, and the corresponding Λ parameters from eq. (30) with dash-dotted lines. Once $\Lambda \gtrsim 2$, the velocity profile approaches the analytic approximation, indicating that the head wobbling motions are small, and the jet propagates similarly to a hydrodynamic jet.

In the high-luminosity jet, the wobbling motions of the head are relatively large at $z_h \lesssim 300$. In this regime, β_h deviates from the analytic solution and has a steeper dependence on z_h . As the jet head propagates to higher altitudes it becomes more stable and the wobbling amplitude decreases. The effective cross-section of the jet decreases with increasing z_h , thus the head velocity increases at a faster rate than the analytic expectation. At $z \gtrsim 300$ the simulated velocity profile is close to the analytic approximation (to within $\sim 10\%$) and exhibits a similar profile, $\beta_h \propto z_h^{1/6}$, reflecting the increased stability of the head to kink modes. In the low-luminosity jet, on the other hand, the wobbling motions remain large until the head reaches the altitude $|z| = 800R_L \simeq 8 \times 10^9$ cm. Therefore the velocity remains below the analytic approximation and follows a steeper z_h -dependence. Based on these two cases, we suggest that the simulated β_h approaches the analytic solution at $\Lambda \gtrsim 2$.

Note that for both high- and low-luminosity jets, at $z_h \lesssim 60$ the head velocity decreases with increasing z_h . This decrease represents early times in the simulation when the jet head just starts to propagate outward and the magnetic field on the surface of the NS is very high due to the buildup of the toroidal magnetic field when the jet was just formed. This leads to an increase in the Pointing flux which pushes the head at a greater force. As the jet begins to propagate, the excess of B_ϕ and the Poynting flux decrease.

Equations (30) and (32) depend on the inverse of $(\rho_a z_h^2)$. Since this expression decreases in density profiles steeper than z^{-2} , in such profiles the jet accelerates and becomes progressively more stable to kink modes with increasing distance. In contrast, in density profiles shallower than z^{-2} , the jet would decelerate and become less stable with the increasing distance from the central compact object. In this case, the propagation velocity would be slower than the one obtained in eq. (32), since the wobbling of the jet head would increase the effective cross-section of the jet. Therefore, the jet would have to push a larger amount of gas to propagate. In such

a case, we expect that there would be some altitude at which the head velocity will be comparable to the expansion velocity of the cocoon, $\sqrt{p_c/\rho_a}$. When this happens, the cocoon would begin to overtake the jet, and we expect that the jet would stall.

8 ASTROPHYSICAL APPLICATIONS

We now consider our analytic model for the jet propagation in the context of two systems that are expected to host magnetised relativistic jets: GRBs and AGN. In the GRB case, we take a jet with a typical power of 3×10^{49} erg/s (e.g. Guetta et al. 2005), that propagates in a fiducial Wolf-Rayet star of mass $M_* = 10M_\odot$, radius $r_* = 10^{11}$ cm, and density profile $\rho_a \propto r^{-\alpha}$, with $\alpha = 2.5$. The stability parameter (eq. 30) of the jet is

$$\Lambda_{\text{GRB}}(z_h) \simeq 2.6 \left(\frac{z_h}{r_*} \right)^{(\alpha-2)/6} \left(\frac{L_{49.5} r_{*,11}}{M_{*,34.3} \gamma_{0.3}^2} \right)^{1/6} \left(\frac{(5-\alpha)^2(3-\alpha)}{3.125} \right)^{1/6} \eta, \quad (33)$$

where $\eta \sim 0.5-1$ (see eq. 29) and we take $\sqrt{\beta_j}/\beta_A \sim 1$. Here, we used the notation $A_x \equiv A \times 10^x$. The inefficient acceleration of the jet material below the head implies that γ_j changes only weakly as a function of the position of the jet head and remains approximately 2 over many decades. Eq. (33), therefore, gives $\Lambda_{\text{GRB}} \approx 2.6$, which suggests that a GRB jet is expected to be only marginally deformed by the external kink instability as it propagates through the star, and that the jet head velocity should not deviate much from the analytic approximation (31) for β_h . The weak dependence of Λ on z_h implies that even close to the light cylinder, at $z_h = 10^7$ cm, Λ_{GRB} remains larger than 1, thus the jet is expected to be marginally stable also in the stellar interior. However, as we see from the simulations, the marginal stability implies substantial wobbling motions that reduce its propagation velocity to below the analytic expectation (31), in regions with $\Lambda \approx 1$. By substituting the GRB parameters into eq. (32), we obtain an estimate of the jet head velocity,

$$\beta_{h,\text{GRB}}(z_h) \simeq 0.3 \left(\frac{z_h}{r_*} \right)^{(\alpha-2)/3} \left(\frac{L_{49.5} r_{*,11} \gamma_{0.3}^4}{M_{*,34.3}} \right)^{1/3} \left(\frac{(5-\alpha)(3-\alpha)^2}{0.625} \right)^{-1/3}, \quad (34)$$

which as we show in Sec. 7, provides a good approximation for the true velocity outside $r \simeq 3 \times 10^9$ cm, or outside of the inner few percents of the stellar radius where $\Lambda \gtrsim 2$. Thus, the propagation velocity of a typical GRB jet in the star is sub-relativistic, and well described by eq. (34).

The breakout time of the jet from the star can be obtained by integrating $\int_0^{R_*} dz/\beta_h c$, which gives $t_b \simeq 10$ sec for the fiducial parameters used here. Bromberg et al. (2012, 2014) showed that the distribution of GRB duration times fits a typical breakout time of the jet from the progenitor star of about 10 sec, in agreement with the breakout time we obtain here. Note that this propagation velocity is somewhat slower than the propagation velocity of an equivalent hydrodynamic jet obtained analytically (Bromberg et al. 2011) and in 2D simulations (e.g. Morsony et al. 2007; Mizuta & Aloy 2009). Although recent 3D simulations of hydrodynamic jets indicate that the two velocities are actually similar (López-Cámara et al. 2013).

When $\Lambda < 1$ the wobbling motions of the jet head due to the external kink are large enough to decrease β_h significantly. As a result, the breakout time of the jet from the star becomes much longer than 10 sec. A typical core-collapse GRB engine is active for at least as long as the GRB lasts (Sari & Piran 1997), or a few tens of seconds (Kouveliotou et al. 1993). If the jet power decreases, the jet becomes less stable and slower, and chances are that the central

engine will shut off before the jet head reaches the stellar edge. In this case, the jet will not be able to break out of the star and will remain buried in it.

Such failed jets are favourable sources for producing low-luminosity GRBs that could occur when the cocoon breaks out of the stellar surface (Kulkarni et al. 1998; MacFadyen et al. 2001; Tan et al. 2001; Wang et al. 2007; Waxman et al. 2007; Katz et al. 2010; Bromberg et al. 2011; Nakar & Sari 2012; Nakar 2015). The minimum power below which the jet becomes kink-unstable in the star is obtained by setting $\Lambda_{\text{GRB}}(r_*) = 1$ in eq. (33), giving a (single) jet power of

$$L_{\text{min}}^{\text{GRB}} \simeq 10^{47} M_{*,34.3} r_{*,11}^{-1} \gamma_{0,3}^2 \left(\frac{3.125}{(5-\alpha)^2(3-\alpha)} \right) \eta^6 \text{ erg/sec.} \quad (35)$$

The associated isotropic equivalent luminosity is $L_{\text{min,iso}}^{\text{GRB}} \simeq 2.6 \times 10^{49} (\theta/7^\circ)^{-2}$ erg/sec, assuming a jet with a characteristic half-opening angle of 10° . A jet with a lower power is less likely to produce a regular GRB (see also Woosley & Zhang 2007). Interestingly, the observed distribution of GRB luminosities shows a cutoff at isotropic equivalent luminosities lower than $\sim 3 \times 10^{49}$ erg/sec (e.g. Cao et al. 2011). A slow, kink-unstable jet, provides a natural explanation for such a cutoff.

After the jet breaks out from the star, the jet head accelerates and loses causal contact with the jet base. The jet, in principle, should relax back to the configuration of a steady state, headless jet that is relatively stable to kink modes and is less likely to undergo internal energy dissipation, as we discussed in Sec. 4. However, at this point the jet is sufficiently wide so that the collimation point is located far outside the light cylinder. In such a case, the poloidal field is too weak to counterbalance the contracting force of the hoop stress, resulting in a large pinching of the jet at the collimation nozzle (see Sec. 6.1). The converging field lines have a large dispersion of pitch angles, and they converge into a small enough region that internal kink modes can grow and efficiently dissipate the magnetic energy, even without the extra compression of toroidal field coming from the jet head. We have run a version of our fiducial model, M3, in which the jet breaks out of a “stellar surface” at $r = 800R_\odot$ and verified that the dissipation at the recollimation nozzle continues long after the breakout. A full analysis of the jet at the post breakout stage will be done in the future.

The jet material that emerges from the star is therefore relativistically hot, with half of its energy in thermal pressure and half still locked in the form of magnetic field. This means that there is sufficient thermal and magnetic energy to accelerate the jet material to high Lorentz factors that are inferred from the observations (see, e.g., Lithwick & Sari 2001; Panaitescu & Kumar 2002). The jet width at that time is of the order $R_j \sim 10^9$ cm (eq. 26) and agrees to an order of magnitude with the inferred size of the emission region in GRB 970828 (Pe’er et al. 2007). The site of the dissipation, which takes place at about $z \sim 10R_j \sim 10^{10}$ cm, is located sufficiently deep in the star, so that the amount of thermal photons required by observations of prompt emissions can be produced (Vurm et al. 2013). Note that the generation of the high energy non-thermal emission, seen in many GRBs, potentially requires an additional dissipation process to take place relatively close to the photosphere, which can lie outside of the star (e.g. Shemi & Piran 1990; Mészáros & Rees 2000; Bromberg et al. 2011). This topic is beyond the present work.

Our results have important implications for AGN jet classification which divides AGN radio galaxies into two types: Fanaroff-Riley type I and II (FRI and FRII) galaxies (Fanaroff & Riley 1974). FRII galaxies show stable jets that typically extend over several

hundred kiloparsecs (e.g. Hardcastle et al. 1998; Godfrey & Shabala 2013), with a well-defined hotspot at the jet head, and a cocoon that extends from the jet head backwards. The jets in FRI galaxies, on the other hand, are much shorter on average, extending over several tens of kiloparsec (e.g. Xu et al. 2000). They emit radiation throughout the jet body, indicative of volumetric dissipation, and their cocoons usually outrun the jet heads. A similar morphology to that of the FRI galaxy jets is expected when the jet head becomes kink unstable and its velocity drops below the expansion velocity of the cocoon. As we show in Sec. 7, this can occur if the jet propagates in a medium with a density profile that is flatter than r^{-2} . Recent studies have shown that the density profiles in clusters of galaxies are relatively flat with $\rho_a \propto r^{-1}$ at the inner part of the cluster ($r \lesssim 100$ kpc) and steepen to $\rho_a \propto r^{-2}$ further out (e.g. Newman et al. 2013). In this case, a jet with a luminosity below

$$L_{\text{min}}^{\text{FR}} \simeq 4 \times 10^{45} \frac{\rho_a}{10^{-26} \frac{\text{g}}{\text{cm}^3}} \left(\frac{r}{100 \text{ kpc}} \right)^2 \left(\frac{\gamma_j}{2} \right)^2 \left(\frac{3.125}{(5-\alpha)^2(3-\alpha)} \right) \eta^6 \text{ erg s}^{-1} \quad (36)$$

will have a stability parameter $\Lambda < 1$ at $r < 100$ kpc and will become unstable to external kink before leaving the inner flat density core. The wobbling motions increase the effective jet cross-section of the jet and reduce the propagation velocity until it becomes comparable to the expansion velocity of the cocoon. From this point on, the jet is effectively stalled. The continuous injection of energy at the jet head results in a prominent, massive cocoon relative to the jet. In addition, the increasing wobbling motions can trigger dissipation along the jets that leads to radiation, making the jets shine and appear as FRI jets. In the opposite case, when $L > L_{\text{min}}^{\text{FR}}$, the jets are able to break out of the core before they become unstable. Once out, they accelerate in the steep density profile outside the galaxy core and become increasingly stable. These jets are expected to have more elongated, less energetic cocoons, and are expected to have well-defined working surfaces at their heads where most of the work is being done to push the ambient medium. Such a morphology is observed in FRII jets.

9 COMPARISON WITH OTHER WORKS

The stability of magnetised jets was studied extensively via 3D simulations, both in local, periodic boxes and in global simulations. In many studies, the jet morphology and the magnetic field configuration (including the pitch angle, or toroidal to poloidal field strength ratio) is prescribed in an ad hoc way. In addition, the jets are usually assumed to be of a cylindrical shape, and some initial perturbations are imposed on the field lines to break the axial symmetry and jump-start the kink instability. This suggests that in such studies jet stability can be sensitive to the details of the initial jet setup (e.g., the parameters of jet injection boundary conditions, the initial conditions with which the jets are initialised, etc.) making it difficult to draw firm conclusions about jet stability. By comparing the properties of our self-consistently launched jets to other works, we can build up intuition on what effect the particular simulation details have on the simulation outcome and where our results fall in the global landscape of simulated jet configurations.

Mizuno et al. (2012) studied the stability of a stationary jet with a poloidal field dominated core surrounded by toroidal field dominated sheath, which extended to the edge of their grid. They tested several configurations of toroidal and poloidal field lines in the sheath which characterised by different values of b_ϕ/b_p . They found that the instability grew faster for steep lateral field profiles

and higher ratios of b_ϕ/b_p . When the lateral toroidal profile in the sheath became flatter than $R^{-1/2}$, the instability grew over a longer timescale and eventually saturated.

Porth & Komissarov (2015) conducted a similar study using jets that contained only toroidal magnetic field with a profile $b_\phi \propto R^{-1}$ outside a core. They replaced the poloidal field with thermal pressure, which dominated the core, was sub-dominant outside, and had a flat profile outside the core (they found that the inclusion of poloidal field had no noticeable stabilising effect). Their jets, which are moderately magnetised, became kink unstable over a time scale that is consistent with the expected growth time, $\sim 10t_{\text{kink}}$. They witnessed that the energy dissipation associated with the kink instability led to an increase in the jet core size, similar to our findings. Since their jets were infinite, the instability could grow in the jet indefinitely, and the jets were eventually disrupted after $\sim 40t_{\text{kink}}$. They also confirmed that the jets remain stable if they expand sideways with a velocity that is fast enough, so that the conditions for strong transverse causal contact are not met. We find that in a time-dependent case, the sideways expansion of the cocoon does lead to an increase in the jet radius with time. However, in the environments that are relevant for GRB and AGN jets, the rate of the expansion is slow, and the jet remains in strong causal contact.

Studies of the energy dissipation processes in stationary, non-relativistic magnetised jets were conducted by Hood et al. (2009); Gordovskyy & Browning (2011) and Pinto et al. (2015) in the context of solar flares. They all considered a cylindrical jet with poloidal field dominated core surrounded by a toroidal field dominated sheath with a profile steeper than $b_\phi \propto R^{-1}$. In their setup the jet is surrounded by a uniform magnetic field in the z -direction, which provides support for the jet from the sides, similar to the effect of the cocoon in our case. In all of their simulations the internal kink evolved in the jet on a time scale comparable to the expected linear growth time, $\sim 10t_{\text{kink}}$. The internal kink resulted in magnetic energy dissipation over a comparable time scale. It led to the dissipation of most of the toroidal component of the field, and to a jet with mostly a poloidal field. This result is consistent with the internal dissipation in our collimated jets.

Global simulations of Poynting dominated jets were conducted by Mignone et al. (2013). They injected a cylindrical jet at the lower boundary of their grid and tracked its propagation. The ambient medium was composed of a spherically symmetric supernova gas that expands homologously into a uniform density medium. The jets were assumed to be cylindrical, with only toroidal field and thermal pressure. The thermal pressure dominated in the core ($R_0 \sim 1/3R_j$), and the toroidal pressure dominated outside the core. They tested jets with several σ parameters and Lorentz factors. Their jets were deformed considerably above $\sim 10t_{\text{kink}}c$, as expected. They also found indications that at the region where magnetic energy was dissipated, field lines became more aligned with the average jet velocity, indicating an effective decrease of toroidal field in the jet. The overall morphology of the jet and its propagation velocity were consistent with our results.

Nakamura et al. (2007) carried out global, non-relativistic MHD simulations of AGN jets propagating in a gravitationally stratified isothermal medium. They injected non-rotating, magnetised jets with a prescribed magnetic pitch $b_\phi/b_p \sim 25$. They found evidence of both internal kink at smaller distances and external kink at larger distances once they perturbed the ambient medium. They did not find any jet heating by the internal kink.

Guan et al. (2014) carried out relativistic MHD simulations of non-rotating jets injected at a distance of $\sim 10^3$ gravitational radii

into a uniform background medium and followed them for about 3 orders of magnitude in distance. The transverse radius of their injected jets was marginally resolved by 2–3 grid cells. They found that when the jet material is injected with ratios of $b_\phi/b_p > 10$ it develops internal kink modes and experiences substantial dissipation of magnetic energy, similar to our work. Above the dissipation regions, their jets seem to be considerably more bodily kinked than ours. This is possibly because they propagate in a uniform density profile that applies a larger resistive force on the jet head than in our case. Similar to our work, they found that the instabilities slowed down the jet propagation but did not disrupt the jets.

On the analytic front, Lyubarsky (2009, 2011) obtained steady state solutions to the structure of collimated Poynting dominated jets. He showed that when the jet is collimated far from the linear acceleration regime, it is focused into a recollimation nozzle due to the excess force of hoop stress. Based on these solutions, Lyubarsky (2010, 2012) postulated that if the recollimation nozzle is narrow enough, strong dissipation should occur which will effectively convert the magnetic into thermal energy. Models for the propagation of a Poynting dominated GRB jet in a star were developed by Levinson & Begelman (2013) and Bromberg et al. (2014). Both groups obtained similar, mildly relativistic values for the velocity of the jet head. However, since they ignored the wobbling motions of the head due to the external kink instability, they overestimated the head velocity. Based on their findings of the jet width, Levinson & Begelman (2013) concluded that the magnetic field is dissipated at the base of the jet, leading to a hydrodynamic jet. Bromberg et al. (2015) reached a similar conclusion based on the short breakout time of the jet from the star that their model predicted. Indeed, we find that efficient dissipation of magnetic energy takes place at the recollimation nozzle, however it affects not all, but about half of the magnetic energy.

10 DISCUSSION AND CONCLUSIONS

In this work we present the results of a global numerical 3D MHD stability study of relativistic Poynting flux dominated jets that propagate in an ambient medium. The stability of a jet largely depends on the way it is launched and the ambient medium it interacts with. In order for our simulations to have predictive power when it comes to jet stability, we set them up to launch the jets in the same way as nature does it: via the magnetised rotation of a central compact object. The magnetised outflow thus produced has a wide opening angle initially. As it interacts with the ambient medium, magnetic pinch forces collimate it into twin narrow oppositely directed near-cylindrical jets. In this way, the structure of the jets is established self-consistently, without any a priori assumptions about, e.g., the jet Lorentz factor, opening angle, or magnetic pitch angle. All of these quantities control jet stability (see Sec. 3) and are determined self-consistently by the jet launching physics. In fact, our models are characterised by just two basic dimensionless parameters describing the astrophysical system: the energy density of the poloidal magnetic field of the central compact object (in units of the ambient gas density) and the slope of the ambient gas density distribution (see Table 2).

We make a distinction between the jets that propagate in an empty, pre-drilled funnel and the jets that have to drill their funnel for themselves. The former, *headless jets*, propagate unobstructed, accelerate to high Lorentz factors, and do not easily show signs of instability. The latter, *headed jets*, have much larger pitch angles (reflecting a stronger toroidal magnetic field component) and

propagate slower due to the need to expend energy on the drilling through the ambient gas; both of these effects make headed jets unstable to current-driven, non-axisymmetric instabilities.

As headed jets run into the ambient medium, they collimate off of it. In fact, they recollimate and rebound, which leads to a nozzle-like shape of the jet (see Fig. 8). We show that recollimation-induced-compression causes the jets to become unstable to the internal kink mode. This instability appears without any perturbations imparted to the jets or the ambient gas and leads to efficient dissipation of the toroidal magnetic field component. The instability operates until the equipartition between thermal and magnetic energies is reached: the thermal pressure stabilises the jets against the further growth of the internal kink (Hood & Priest 1979), and the dissipation stops at plasma $\beta = p_{\text{th}}/p_{\text{mag}} \sim 1$.

We find that the dissipation rate is comparable to the growth rate of the internal kink modes, with most of the dissipation taking place close to the recollimation point. Our simulations do not include explicit resistivity. Encouragingly, we find that the dissipation rate is rather insensitive to the numerical resolution. The rate is consistent with that found in resistive MHD simulations of internal kink instability in the context of solar flares (e.g. Hood et al. 2009; Gordovskyy & Browning 2011; Pinto et al. 2015) and ideal relativistic MHD simulations of steady state jets in periodic boxes (e.g. Mizuno et al. 2012; O’Neill et al. 2012). It is therefore possible that in some cases the dissipation rate can be determined by the rate at which the macroscopic instability creates and brings together field lines of opposite polarity and is rather insensitive to reconnection microphysics.

We stress that whereas in our simulations jet recollimation leads to dissipation, the nature of dissipation is different from the usual picture of dissipation at a recollimation shock in a hydrodynamic jet (Gomez et al. 1995; Marscher et al. 2008; Bromberg & Levinson 2009; Nalewajko & Sikora 2009; Meier 2012; Nalewajko 2012; Nalewajko & Sikora 2012; Cohen et al. 2014). Even highly magnetised jets can undergo a recollimation shock provided the jet is super-fast magnetosonic. However, not much dissipation occurs at the shock itself, and instead the dissipation happens due to the activation of the internal kink instability in the post-shock/post-recollimation region: at the shock, the flow velocity decreases and b_ϕ increases, both of which encourage the development of an internal kink mode. In the context of AGN, such a jet recollimation can be responsible for bright features seen in the jets at around the Bondi radius: for instance, the HST-1 component in the M87 jet (Biretta et al. 1999; Meyer et al. 2013; Hada et al. 2015) could be caused by the dissipation via the internal kink mode near the recollimation point where the jet starts interacting with the interstellar medium and the bright components emerging from and/or passing through HST-1 might be the dissipation sites caused by the kink instability.

The jets emerge from the dissipation region with the toroidal magnetic field component greatly weakened and the thermal jet content much boosted by the dissipation. This has a stabilising effect on the internal kink mode and causes the dissipation to be localised near the jet recollimation point. This dissipation continues long after the jets break out of the star (see Sec. 6.2). Since the magnetic energy is dissipated deep inside the star, the emerging plasma contains enough photons to account for the GRB emission (Vurm et al. 2013). However, the non-thermal emission observed in many GRBs likely requires additional dissipation to occur close to or beyond the photosphere (see, e.g., Giannios 2008). This can happen if the plasma cools by adiabatic expansion or sub-photospheric emission and regains high enough magnetisation for the internal kink

mode to be revived. It is also conceivable that if the plasma undergoes a rapid expansion phase when exiting the star, parts of it may attain a low enough magnetisation (Tchekhovskoy et al. 2010b), and the internal shocks may become effective; however, it is unclear if these parts carry sufficient amounts of energy to power the prompt emission. Additional magnetic dissipation can be expected if the magnetic flux threading the jets switches polarity (e.g. Drenkhahn & Spruit 2002; Giannios & Spruit 2005; Narayan et al. 2011; McKinney & Uzdensky 2012; Deng et al. 2015), either due to the oblique magnetic field of a central magnetar producing a striped wind (Metzger et al. 2011) or due to the accretion of matter with alternating magnetic field polarity onto the central BH (e.g., Tchekhovskoy & Giannios 2014; Parfrey et al. 2015).

We find that the jet residual magnetic field content beyond the recollimation point is sufficient to trigger the external kink instability, which leads to large-scale helical motions and bends, causing the jet head to wobble (see Fig. 14). As a result, the effective cross-section of the jets increases and the jet propagation velocity decreases. Using an analytic model, we show that the stability of our relativistically-hot jets to the external kink mode is controlled by the following dimensionless parameter,

$$\Lambda \propto \left(\frac{L_j}{\rho_a z_h^2 \gamma_j^2 c^3} \right)^{1/6},$$

where ρ_a is the ambient density, z_h is the distance to the jet head, and γ_j is the Lorentz factor of jet material (which is larger than that of the jet head; see Sec. 7). When Λ substantially exceeds unity, the external kink does not have sufficient time to evolve in the jets, and the wobbling motions remain small. In this case, the jets propagate at a similar velocity to hydrodynamic jets. However, when $\Lambda \lesssim 1$, the jet heads become unstable to external kink modes. The jet head velocity significantly decreases and becomes much smaller than that of hydrodynamic jets. Using our analytic model, we show the stability of the jets and the propagation velocity of their heads are closely related to the profile of the external density. In ambient density profiles steeper than $\rho \propto r^{-2}$, the jets accelerate and become more stable with increasing distance. In flatter profiles, however, the jets decelerate and become exceedingly unstable. We expect that eventually the head velocity becomes comparable to the expansion velocity of the shocked external gas, which then outruns the jets. This may cause the jets to stall.

The concept of a stalled jet can explain the difference in the morphology of FRI and FRII radio galaxy jets (Fanaroff & Riley 1974). The jets of FRI galaxies usually extend to several tens of kpc, are engulfed in a massive cocoon, and shine along the entire body. FRII galaxy jets, on the other hand, are much longer on average ($\gtrsim 100$ kpc), maintain straight course and have a well-defined, bright, hot spot at the jet head. These differences can be explained via the effects of the external kink instability. In the flat density profiles of galaxy cluster cores, the jets decelerate as they propagate outwards. Therefore, a minimal power exists above which they are able to break out of these cores. We estimate this minimal power to be $L_{\text{min}}^{\text{FR}} \sim 4 \times 10^{45}$ erg s $^{-1}$, adopting typical properties of radio galaxies (see Sec. 8 and Tab. 2). Jets with a lower power become external-kink-unstable inside the core. They develop wobbling motions which increase their effective cross-section and cause them to slow down until they are overrun by their cocoons that continuously expand. The increased wobbling motions can also trigger dissipation along the jets that leads to radiation, making the jets shine and appear as FRI jets. A higher luminosity jet will break out of the flat density core before becoming highly kink-unstable and will continue to accelerate in the steep ambient density profile that

surrounds the galaxy core. Such a jet will remain stable and will appear as an FR II jet.

In the GRB case, the density profile of the stellar envelope is so steep that the jets become exceedingly more stable as they propagate outward. We find that typical GRB jets are marginally stable and propagate at a velocity $\lesssim 0.5c$, similar to the velocity of hydrodynamic jets (see Fig. 17). They break out of the star in about ~ 10 seconds. Bromberg et al. (2015) concluded that Poynting flux dominated jets need to dissipate their energy close to the source in order for the breakout time to be consistent with observations. We show here that such a dissipation mechanism indeed exists near the recollimation point of the jet. The breakout time agrees with that inferred from the distribution of GRB duration times (Bromberg et al. 2012, 2015). The similarity between the propagation velocities of hydrodynamic and our relativistically-hot MHD jets suggests that it is difficult if not impossible to distinguish between magnetic and hydrodynamic energy injection mechanisms in the jets based on the observed breakout time alone.

We find that if the power of a (single) GRB jet drops below $\sim 10^{47}$ erg s^{-1} , which corresponds to an isotropic equivalent luminosity of $\sim 2.6 \times 10^{49} (\theta/7^\circ)^{-2}$, the jet becomes so strongly unstable to the external kink mode inside the star that its propagation velocity significantly drops (see Sec. 8). This can lead to a situation where the GRB engine shuts off before the jet is able to breakout of the star. In this case, only the cocoon breaks out of the star, and feasibly leads to a different type of burst, which may resemble a low-luminosity GRB (Kulkarni et al. 1998; MacFadyen et al. 2001; Tan et al. 2001; Wang et al. 2007; Waxman et al. 2007; Katz et al. 2010; Bromberg et al. 2011; Nakar & Sari 2012; Nakar 2015).

We note that whereas our simulations are carried out for a neutron star as the central compact object, our results are applicable to the case of an accreting black hole. This is because both black holes and neutron stars launch the jets via the azimuthal winding of poloidal magnetic field lines, as we discussed previously. The difference is that the field line winding in the case of the neutron star is due to the rotation of an actual, physical surface with magnetic field lines frozen into it, and in the black hole case it is due to the rotation of the space-time (Tchekhovskoy 2015). Note, however, that the presence of a black hole accretion disc, which we do not include in this work, may change the conditions at the base of the jet and affect the jet structure. For instance, a disc wind may alter the confining pressure profile of the jet. These effects will be studied elsewhere.

In this work, we only studied jet propagation for 3 orders of magnitude in distance. This is short by about an order of magnitude in distance of the actual stellar surface. Carrying out longer-term simulations that extend up to and beyond the stellar surface are important for verifying the stability of the jet out to larger distances and testing our analytic models in this new regime. We have not studied the processes that occur in the jets upon their breakout of the star. The breakout can be accompanied with substantial acceleration (Tchekhovskoy et al. 2010b) and the loss of causal contact across the jet (Komissarov et al. 2010), both of which can affect the development of the instability. The simulations of jet breakout are important also in order to compute a first-principles structure of the jet outside of the star to improve the GRB prompt and afterglow emission modelling.

The main finding of this work is the efficient dissipation of the jet magnetic field near the recollimation point via the internal kink instability. Though the dissipation rate is presently difficult to measure quantitatively due to the inherent time variability and potential sensitivity to the microphysics, the outcome of the inter-

nal kink instability—a hot jet with thermal and magnetic energies in equipartition—is robust. It was obtained by multiple groups in various contexts using different numerical methods. Thus, the jet material that emerges from the star is both relativistically-hot and relativistically-magnetised. We conclude that the internal kink instability leads to jets that have enough magnetic and thermal energy to accelerate to the highly relativistic Lorentz factors inferred for GRBs, and carry a substantial thermal energy flux, which can be used to power the prompt emission.

ACKNOWLEDGMENTS

We thank R. Barniol Duran, E. Blackman, D. Giannios, H. Li, Y. Lyubarsky, J. McKinney, R. Narayan, K. Parfrey, A. Philippov, S. Phinney, E. Quataert, F. Ryde, and A. Spitkovsky for discussions that helped us to improve this work. O.B. acknowledges support from the Lyman Spitzer Jr. Fellowship, awarded by the Department of Astrophysical Sciences at Princeton University and the Max-Planck/Princeton Center for Plasma Physics which facilitated this work. A.T. was supported by NASA through Einstein Postdoctoral Fellowship grant number PF3-140115 awarded by the Chandra Xray Center, which is operated by the Smithsonian Astrophysical Observatory for NASA under contract NAS8-03060, and NSF through an XSEDE computational time allocation TG-AST100040 on NICS Kraken, Nautilus, TACC Stampede, Maverick, and Ranch. The simulations presented in this work also used computational resources supported by the PICSciE-OIT High Performance Computing Center and Visualization Laboratory, and the Savio cluster provided by UCB.

APPENDIX A: ANALYTIC MODEL OF THE JET

In this Appendix we calculate the jet radius following the calculation method of Bromberg et al. (2011), with some minor modifications to fit the specific model of the magnetised jet. As illustrated in Fig. 16, we assume a cylinder-shaped jet surrounded by a cylindrical cocoon propagating in a cold medium. The jet propagates in the z -direction and injects energy into the cocoon at the outermost parts jet of the jet, or at the *jet head*. As a result the cocoon becomes pressurised and expands sideways into the ambient medium, as seen in Figure 16. The calculation here is relevant for an external medium density with a power-law profile: $\rho_a \propto z^{-\alpha}$. The power-law assumption implies that all the quantities in the problem have a power-law dependency on z as well, which makes it easier to integrate them.

According to eq. (19) the cocoon pressure is

$$p_c = \frac{E_c}{3V_c} = \frac{\int L_j(\beta_j - \beta_h) dt}{3\pi \int \beta_h dt \left(\int \beta_c dt \right)^2}, \quad (\text{A1})$$

where β_h is the velocity of the jet head and β_j is the velocity of the jet material that lies below the head and that carries the jet energy to the head. L_j is the power, or luminosity, injected into the jet by the engine located at the base of the jet and the term $L_j(\beta_j - \beta_h)$ represents the fraction of that luminosity that reaches the jet head and is injected into the cocoon. β_c is the average expansion velocity of the cocoon in the transverse direction. Since the cocoon expands into a cold gas, it drives a shock into the ambient medium. We can approximate the expansion velocity of the cocoon as the velocity of that shock: $\beta_c = \sqrt{p_c / \bar{\rho}_a c^2}$, where $\bar{\rho}_a$ is the average ambient density along the shock's upstream. Substituting this expression in

eq. (A1), we get (up to integration constants, which can be calculated posteriorly):

$$p_c \approx \sqrt{\frac{\bar{\rho}_a c^2 L_j (\beta_j - \beta_h)}{3\pi\beta_h t^2}}, \quad (\text{A2})$$

Following Matzner (2003); Bromberg et al. (2011) we define a dimensionless parameter

$$\tilde{L} \equiv \frac{L_j}{\pi R_j^2 \rho_a c^3} = \left(\frac{\beta_j - \beta_h}{\beta_h} \right)^2, \quad (\text{A3})$$

where R_j is the cylindrical radius of the jet. Substituting eq. (A3) in eq. (A2), and defining $t \approx z_h/\beta_h c$, where z_h is the distance to the jet head, we get (up to a constant)

$$p_c \approx \left(\frac{\bar{\rho} L_j}{\pi c} \right)^{1/2} \tilde{L}^{-1/4} t^{-1} = \left(\frac{\bar{\rho}_a L_j c}{\pi z_h^2} \right)^{1/2} \left(\frac{L_j}{\pi R_j^2 \rho_a c^3} \right)^{1/4} \quad (\text{A4})$$

The cocoon maintains a pressure balance with the jet along the jet edge (at R_j). We can calculate $p_j(R_j)$ the equation for the total jet power:

$$L_j = 2\pi \int_0^{R_j} \frac{\Gamma}{\Gamma - 1} p_j \gamma_j^2 \beta_j c R dR, \quad (\text{A5})$$

where the p_j is given in eq. (23) and Γ is the adiabatic index. To calculate Γ we can write the total jet pressure as the sum of the thermal pressure and the magnetic pressure:

$$p_j = (\Gamma_{\text{th}} - 1)u_{\text{th}} + (\Gamma_{\text{mag}} - 1)u_{\text{mag}} = \frac{1}{3}u_{\text{th}} + u_{\text{mag}}, \quad (\text{A6})$$

where Γ_{th} (Γ_{mag}) and u_{th} (u_{mag}) are the adiabatic index and the energy density of the gas (magnetic field) respectively. In Sec. 6.2 we show that above the dissipation region the thermal and magnetic pressures are in equipartition, implying that $u_{\text{th}} = 3u_{\text{mag}}$. Substituting that in eq. (A6) we get that

$$p_j = \frac{1}{2}(u_{\text{th}} + u_{\text{mag}}), \quad (\text{A7})$$

This gives an adiabatic index inside the jet of

$$\Gamma = \frac{p_j}{u_{\text{th}} + u_{\text{mag}}} + 1 = \frac{3}{2}. \quad (\text{A8})$$

Integrating eq. (A5) with Γ from (A8) we get that the jet pressure at R_j is

$$p_j(R_j) \approx \frac{2L_j}{9\pi\gamma_j^2\beta_j R_j^2 c}. \quad (\text{A9})$$

The balance between the jet pressure and the cocoon pressure at the jet edge implies, $p_c(R_j) = p_j(R_j)$. Using eqn. (A4) and (A9) we get:

$$R_j \gamma_j = \left(\frac{L_j z_h^4}{\rho_a c^3 \gamma_j^2 \beta_j^3} \right)^{1/6} \sqrt{\frac{2}{9\pi\beta_j} \left(\frac{3\pi(5-\alpha)(3-\alpha)}{2 \cdot 9} \right)^{1/3}}, \quad (\text{A10})$$

where we included the numerical factor obtained from the integrations and defined ρ_a as the ambient density at z_h . To calculate the numerical factor we used the following relations (see Bromberg et al. 2011, appendix B): $\bar{\rho}_a = \int \rho_a dV/V = \frac{3}{3-\alpha}\rho_a$; $z_h = \int \beta_h t = \frac{5-\alpha}{3}\beta_h t$ and $R_c = \int \beta_c dt = \frac{5-\alpha}{3}\beta_c t$.

REFERENCES

Appl S., Lery T., Baty H., 2000, *A&A*, 355, 818

- Begelman M. C., 1998, *ApJ*, 493, 291
 Begelman M. C., Li Z.-Y., 1994, *ApJ*, 426, 269
 Beloborodov A. M., 2010, *MNRAS*, 407, 1033
 Beskin V. S., 1997, *Soviet Physics Uspekhi*, 40, 659
 Beskin V. S., Kuznetsova I. V., Rafikov R. R., 1998, *MNRAS*, 299, 341
 Beskin V. S., Zakamska N. L., Sol H., 2004, *MNRAS*, 347, 587
 Biretta J. A., Sparks W. B., Macchetto F., 1999, *ApJ*, 520, 621
 Blandford R. D., Znajek R. L., 1977, *MNRAS*, 179, 433
 Bogovalov S., Tsinganos K., 2005, *MNRAS*, 357, 918
 Bromberg O., Granot J., Lyubarsky Y., Piran T., 2014, *MNRAS*, 443, 1532
 Bromberg O., Granot J., Piran T., 2015, *MNRAS*, 450, 1077
 Bromberg O., Levinson A., 2009, *ApJ*, 699, 1274
 Bromberg O., Mikolitzky Z., Levinson A., 2011, *ApJ*, 733, 85
 Bromberg O., Nakar E., Piran T., 2011, *ApJ*, 739, L55
 Bromberg O., Nakar E., Piran T., Sari R., 2011, *ApJ*, 740, 100
 Bromberg O., Nakar E., Piran T., Sari R., 2012, *ApJ*, 749, 110
 Bucciantini N., Quataert E., Metzger B. D., Thompson T. A., Arons J., Del Zanna L., 2009, *MNRAS*, 396, 2038
 Burrows A., Dessart L., Livne E., Ott C. D., Murphy J., 2007, *ApJ*, 664, 416
 Cao X.-F., Yu Y.-W., Cheng K. S., Zheng X.-P., 2011, *MNRAS*, 416, 2174
 Cohen M. H., Meier D. L., Arshakian T. G., Homan D. C., Hovatta T., Kovalev Y. Y., Lister M. L., Pushkarev A. B., Richards J. L., Savolainen T., 2014, *ApJ*, 787, 151
 Deng W., Li H., Zhang B., Li S., 2015, *ApJ*, 805, 163
 Drenkhahn G., Spruit H. C., 2002, *A&A*, 391, 1141
 Eichler D., 1993, *ApJ*, 419, 111
 Fanaroff B. L., Riley J. M., 1974, *MNRAS*, 167, 31P
 Giannios D., 2008, *A&A*, 480, 305
 Giannios D., 2012, *MNRAS*, 422, 3092
 Giannios D., Spruit H. C., 2005, *A&A*, 430, 1
 Godfrey L. E. H., Shabala S. S., 2013, *ApJ*, 767, 12
 Gomez J. L., Marti J. M. A., Marscher A. P., Ibanez J. M. A., Marcaide J. M., 1995, *ApJ*, 449, L19
 Gordovskyy M., Browning P. K., 2011, *ApJ*, 729, 101
 Granot J., Komissarov S. S., Spitkovsky A., 2011, *MNRAS*, 411, 1323
 Guan X., Li H., Li S., 2014, *ApJ*, 781, 48
 Guetta D., Piran T., Waxman E., 2005, *ApJ*, 619, 412
 Hada K., Giroletti M., Giovannini G., Casadio C., Beilicke M., Cesarini A., Cheung T., Doi A., Gómez J. L., Krawczynski H., Kino M., Nagai H., 2015, *ArXiv:1504.01808*
 Hardcastle M. J., Alexander P., Pooley G. G., Riley J. M., 1998, *MNRAS*, 296, 445
 Heger A., Langer N., Woosley S. E., 2000, *ApJ*, 528, 368
 Hood A. W., Browning P. K., van der Linden R. A. M., 2009, *A&A*, 506, 913
 Hood A. W., Priest E. R., 1979, *Sol. Phys.*, 64, 303
 Katz B., Budnik R., Waxman E., 2010, *ApJ*, 716, 781
 Kawanaka N., Piran T., Krolik J. H., 2013, *ApJ*, 766, 31
 Kennel C. F., Coroniti F. V., 1984, *ApJ*, 283, 710
 Komissarov S. S., 2001, *MNRAS*, 326, L41
 Komissarov S. S., Barkov M. V., Vlahakis N., Königl A., 2007, *MNRAS*, 380, 51
 Komissarov S. S., Vlahakis N., Königl A., 2010, *ArXiv:0912.0845*
 Kouveliotou C., et al., 1993, *ApJ*, 413, L101
 Kulkarni S. R., Frail D. A., Wieringa M. H., Ekers R. D., Sadler

- E. M., Wark R. M., Higdon J. L., Phinney E. S., Bloom J. S., 1998, *Nature*, 395, 663
- Leng M., Giannios D., 2014, *MNRAS*, 445, L1
- Levinson A., 2006, *International Journal of Modern Physics A*, 21, 6015
- Levinson A., Begelman M. C., 2013, *ApJ*, 764, 148
- Lithwick Y., Sari R., 2001, *ApJ*, 555, 540
- López-Cámara D., Morsony B. J., Begelman M. C., Lazzati D., 2013, *ApJ*, 767, 19
- Lynden-Bell D., 1996, *MNRAS*, 279, 389
- Lyubarskii Y. E., 1999, *MNRAS*, 308, 1006
- Lyubarskij Y. E., 1992, *Soviet Astronomy Letters*, 18, 356
- Lyubarsky Y., 2009, *ApJ*, 698, 1570
- Lyubarsky Y., 2011, *Phys. Rev. E*, 83, 016302
- Lyubarsky Y. E., 2010, *MNRAS*, 402, 353
- Lyubarsky Y. E., 2012, *MNRAS*, 427, 1497
- Lyutikov M., Blandford R., 2003, *ArXiv:astro-ph/0312347*
- MacFadyen A. I., Woosley S. E., 1999, *ApJ*, 524, 262
- MacFadyen A. I., Woosley S. E., Heger A., 2001, *ApJ*, 550, 410
- Marscher A. P., Jorstad S. G., D’Arcangelo F. D., Smith P. S., et al., 2008, *Nature*, 452, 966
- Matzner C. D., 2003, *MNRAS*, 345, 575
- McKinney J. C., Blandford R. D., 2009, *MNRAS*, 394, L126
- McKinney J. C., Uzdensky D. A., 2012, *MNRAS*, 419, 573
- Meier D. L., 2012, *Black Hole Astrophysics: The Engine Paradigm*. Springer, Verlag Berlin Heidelberg
- Mészáros P., Rees M. J., 2000, *ApJ*, 530, 292
- Mészáros P., Rees M. J., 2011, *ApJ*, 733, L40
- Metzger B. D., Giannios D., Thompson T. A., Bucciantini N., Quataert E., 2011, *MNRAS*, 413, 2031
- Meyer E. T., Sparks W. B., Biretta J. A., Anderson J., Sohn S. T., van der Marel R. P., Norman C., Nakamura M., 2013, *ApJ*, 774, L21
- Mignone A., Rossi P., Bodo G., Ferrari A., Massaglia S., 2010, *MNRAS*, 402, 7
- Mignone A., Striani E., Tavani M., Ferrari A., 2013, *MNRAS*, 436, 1102
- Mimica P., Giannios D., Aloy M. A., 2010, *MNRAS*, 407, 2501
- Mizuno Y., Lyubarsky Y., Nishikawa K.-I., Hardee P. E., 2009, *ApJ*, 700, 684
- Mizuno Y., Lyubarsky Y., Nishikawa K.-I., Hardee P. E., 2012, *ApJ*, 757, 16
- Mizuta A., Aloy M. A., 2009, *ApJ*, 699, 1261
- Moll R., 2009, *A&A*, 507, 1203
- Moll R., Spruit H. C., Obergaulinger M., 2008, *A&A*, 492, 621
- Morsony B. J., Lazzati D., Begelman M. C., 2007, *ApJ*, 665, 569
- Mösta P., Richers S., Ott C. D., Haas R., Piro A. L., Boydston K., Abdikamalov E., Reisswig C., Schnetter E., 2014, *ApJ*, 785, L29
- Nakamura M., Li H., Li S., 2007, *ApJ*, 656, 721
- Nakar E., 2015, *ApJ*, 807, 172
- Nakar E., Sari R., 2012, *ApJ*, 747, 88
- Nalewajko K., 2012, *MNRAS*, 420, L48
- Nalewajko K., Sikora M., 2009, *MNRAS*, 392, 1205
- Nalewajko K., Sikora M., 2012, *A&A*, 543, A115
- Narayan R., Kumar P., Tchekhovskoy A., 2011, *MNRAS*, 416, 2193
- Narayan R., Li J., Tchekhovskoy A., 2009, *ApJ*, 697, 1681
- Narayan R., McKinney J. C., Farmer A. J., 2007, *MNRAS*, 375, 548
- Newman A. B., Treu T., Ellis R. S., Sand D. J., Nipoti C., Richard J., Jullo E., 2013, *ApJ*, 765, 24
- O’Neill S. M., Beckwith K., Begelman M. C., 2012, *MNRAS*, 422, 1436
- Panaitescu A., Kumar P., 2002, *ApJ*, 571, 779
- Parfrey K., Giannios D., Beloborodov A. M., 2015, *MNRAS*, 446, L61
- Pe’er A., Ryde F., Wijers R. A. M. J., Mészáros P., Rees M. J., 2007, *ApJ*, 664, L1
- Phinney E. S., 1982, *MNRAS*, 198, 1109
- Pinto R. F., Vilmer N., Brun A. S., 2015, *A&A*, 576, A37
- Piran T., Shemi A., Narayan R., 1993, *MNRAS*, 263, 861
- Porth O., Komissarov S. S., 2015, *MNRAS*, 452, 1089
- Sari R., Piran T., 1997, *ApJ*, 485, 270
- Shemi A., Piran T., 1990, *ApJ*, 365, L55
- Tan J. C., Matzner C. D., McKee C. F., 2001, *ApJ*, 551, 946
- Tchekhovskoy A., 2015, in Contopoulos I., Gabuzda D., Kylafis N., eds, *Astrophysics and Space Science Library Vol. 414 of Astrophysics and Space Science Library, Launching of Active Galactic Nuclei Jets*. pp 45, doi: 10.1007/978-3-319-10356-3_3
- Tchekhovskoy A., Giannios D., 2014, *ArXiv e-prints*
- Tchekhovskoy A., McKinney J. C., Narayan R., 2008, *MNRAS*, 388, 551
- Tchekhovskoy A., McKinney J. C., Narayan R., 2009, *ApJ*, 699, 1789
- Tchekhovskoy A., Narayan R., McKinney J. C., 2010a, *ApJ*, 711, 50
- Tchekhovskoy A., Narayan R., McKinney J. C., 2010b, *New Astronomy*, 15, 749
- Tchekhovskoy A., Philippov A., Spitkovsky A., 2015, *ArXiv:1503.01467*
- Thorne K. S., Price R. H., MacDonald D. A., 1986, *Black holes: The membrane paradigm*. *Black Holes: The Membrane Paradigm*
- Tomimatsu A., 1994, *PASJ*, 46, 123
- Vurm I., Lyubarsky Y., Piran T., 2013, *ApJ*, 764, 143
- Wang X.-Y., Li Z., Waxman E., Mészáros P., 2007, *ApJ*, 664, 1026
- Waxman E., Mészáros P., Campana S., 2007, *ApJ*, 667, 351
- Woosley S. E., 1993, *ApJ*, 405, 273
- Woosley S. E., Zhang W., 2007, *Royal Society of London Philosophical Transactions Series A*, 365, 1129
- Xu C., Baum S. A., O’Dea C. P., Wrobel J. M., Condon J. J., 2000, *AJ*, 120, 2950
- Zamaninasab M., Clausen-Brown E., Savolainen T., Tchekhovskoy A., 2014, *Nature*, 510, 126